Materials & Design 229 (2023) 111895

Contents lists available at ScienceDirect

Materials & Design

journal homepage: www.elsevier.com/locate/matdes

# Design of hierarchical microstructures with isotropic elastic stiffness

Xue Yu [a], Fengwen Wang [b], Zhen Luo [c], Zhan Kang [a], Yiqiang Wang [a,*]

[a] State Key Laboratory of Structural Analysis, Optimization and CAE Software for Industrial Equipment, Dalian University of Technology, Dalian 116024, China
[b] Department of Civil and Mechanical Engineering, Solid Mechanics, Technical University of Denmark, DK-2800 Lyngby, Denmark
[c] School of Mechanical and Mechatronic Engineering, University of Technology Sydney, Sydney, NSW 2007, Australia

## HIGHLIGHTS

- A family of isotropic hierarchical microstructures (Iso-HMs) are designed, which realize isotropic stiffness by synergistic deformations of the members in two levels.
- Iso-HMs gain improved buckling strength, which can reach a hundred times higher than their single-level counterparts.
- The designed Iso-HMs are 3D printed and tested, where the size difference between the specimens and the minimal features reaches over 400:1.

## GRAPHICAL ABSTRACT

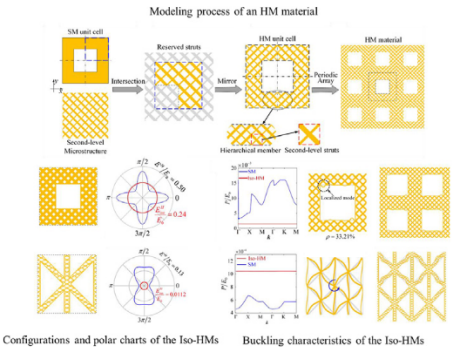


Configurations and polar charts of the Iso-HMs  Buckling characteristics of the Iso-HMs

## ARTICLE INFO

*Article history:*
Received 31 January 2023
Revised 21 March 2023
Accepted 30 March 2023
Available online 6 April 2023

*Keywords:*
Mechanical metamaterial
Hierarchical microstructure
Isotropic stiffness
Microstructural instability
Additive Manufacturing

## ABSTRACT

Elastic stiffness is one of the most fundamental properties of materials. Design of the microstructures with isotropic stiffness has been an attractive area in the field of metamaterials for over three decades. Despite many classes of isotropic microstructures, exploring novel isotropic microstructures based on innovative mechanics principles has attracted great and continuing interests. This paper presents a novel family of isotropic hierarchical microstructures (Iso-HMs). These hierarchical microstructures are modeled by replacing the solid parts of prescribed single-level microstructures with arrayed microstructures in the second level, where the key task is to identify the correct geometries of the second-level microstructures by conducting parameter space exploring. These Iso-HMs realize isotropic stiffness based on synergistic deformations of the members in the two levels, which is essentially different from existing isotropic microstructures replying on deformations of the members in a single level. Two categories of Iso-HMs with rectangular holes and Vidergauze-type struts are designed. Considering the large size difference in the designed Iso-HMs, additive manufacturing becomes a unique technique for manufacturing the designed Iso-HMs, where the size ratio between the 3D-printed specimens and the minimal features reaches 400:1. Both numerical and experimental results validate the isotropic stiffness of the designed Iso-HMs. Furthermore, the results of a microstructural instability analysis show that the designed Iso-HMs can gain improved buckling strength up to a hundred times higher than their single-level counterparts. The hierarchical design provides a new way to identify novel functional microstructures for applications, and the hierarchical configurations expand the space of the already-known families of isotropic microstructures.



* Corresponding author.
*E-mail address:* wangyq@dlut.edu.cn (Y. Wang).

https://doi.org/10.1016/j.matdes.2023.111895
0264-1275/

## 1. Introduction

Microstructured metamaterials gain extraordinary properties through a rational design of microstructure geometries [1–3]. Besides other physical properties, mechanical metamaterials have been designed to attain unusual mechanical properties, such as negative Poisson's ratios [4,5], superior stiffness/strength-to-weight [6], penta-modes [7,8], compression-twisting properties [9,10]. Among all the mechanical properties, the effective stiffness is regarded as one of the most crucial and fundamental microstructural properties desired by potential applications, since it not only determines the overall deformation responses but also affects structural failure strength and many other properties. Particularly, the microstructures with isotropic stiffness are much preferred in engineering, because they have equal stiffness along all directions and are therefore less sensitive to loading uncertainty than anisotropic microstructures. Design of novel isotropic microstructures has attracted great and continuing interests from researchers.

To date, many isotropic microstructures have been designed based on mechanics principles. For instance, Wang and Sigmund [11] designed a family of quasiperiodic isotropic microstructures, the geometries of which meet $n$-fold ($n \geq 5$) rotational symmetries. A rank microstructure was theoretically constructed by layering six sets of members in a rotationally symmetric manner at six separated length scales, but it cannot be practically manufactured due to limitations from multiscale features [12]. Recently, Berger et al. [13] designed a 3D microstructure by combining a simple cubic microstructure and a body-centered cubic microstructure, which realizes nearly-isotropic elastic stiffness by making full use of the complementary variations of the orthotropic stiffness of the two microstructures. Later, Tancogne-Dejean et al. [14] developed a family of combined isotropic microstructures, which synthesized two or three elementary cubic microstructures including the simple cubic, body-centered cubic, and face-centered cubic microstructures in right proportions. This design strategy was also extended to combine shell-like and plate microstructures to achieve stiffness isotropy [15,16]. Both the combined and rotationally symmetric isotropic microstructures can be used for 3D truss and plate microstructures, and they are in theory able to attain the stiffness upper bounds for the Young's, bulk, and shear moduli [11,13,14,16].

Isotropic microstructures can also be designed by using numerical methods. One way is to design parameters or shapes of specific microstructures with fixed configurations. For instance, hollowed struts were used instead of solid struts in elementary microstructures, where the interior and exterior radii of the struts were varied to realize isotropic stiffness [17]. Ma et al. [18] designed isotropic shell lattices with uniform thicknesses by solving a constrained shape optimization problem. Soyarslan et al. [19] obtained isotropic stiffness by tuning the parameters in the approximate representation of minimal surfaces to vary shell shapes. Alternatively, the structural topology optimization methodology is used to design isotropic microstructures with extreme or desired effective properties [20]. The isotropy is ensured either by imposing a constraint or by making use of structural symmetries [21,22]. For now, topology optimization has been used to successfully design the isotropic microstructures with maximal bulk or shear modulus [23,24], maximal bulk and minimal shear modulus [25], penta-mode/bi-mode modulus [8,26], negative Poisson's ratios [5,27], and compression-twisting behaviors [28].

It is noted that the above isotropic microstructures comprise member features in a single level. Differently, hierarchical modeling opens another design dimension, where the hierarchical microstructures (HMs) comprise geometric features in two levels and the hierarchical members in the first level include arrayed microstructures in the second level. In the HMs, the size of the second-level members can be several orders lower than that of the HM unit cell [29]. Moreover, the second-level microstructures could either have similar geometries as the first-level configurations [30] or include spatially-varying configurations. Compared to the multiscale microstructures in which the microstructures in the smaller length scale behave as a homogeneous material for the members in the larger length scale [12], the hierarchical members in HMs perform as structures. Additive manufacturing has become a powerful tool for manufacturing lattice structures with high resolutions and qualities [2,3,31–33]. Particularly, as the HMs are usually intricate and consist of different levels of members with a large size difference, their fabrication becomes challenging for conventional manufacturing technologies. In this sense, additive manufacturing provides a unique technology for manufacturing HMs in an integrated manner [34]. Many attempts have been made for 3D printing HMs, whose feature sizes can span over four to six length orders from tens of millimeters to several nanometers [34–36].

HMs are able to gain many excellent properties that can be hardly found in single-level microstructures (SMs). For instance, various classes of auxetic HMs have been designed by achieving the hierarchy either in each level of cells or in the whole microstructures [37]. The HMs can have either honeycomb-like geometries [38], re-entrant-type configurations [39] or rotating units [40]. These auxetic HMs can gain enhanced mechanical characteristics, including the high shear stiffness, fracture toughness among others [40–43]. Furthermore, many other HMs have been designed for realizing high resistance to brittle failure [44,45], high strength [29,34,35], and superior energy absorption capabilities [46]. These superior properties can be attributed to the collaborative advantages of structures from two levels. The results from topology optimization also validate that the optimal design with the target of maximizing the buckling strength yields HM solutions [47]. Even though many existing HMs, a systematic design of HMs for pursuing isotropic stiffness has yet to be studied.

In this paper, a new type of isotropic microstructures is obtained through a hierarchical design methodology, which is called the isotropic hierarchical microstructures (Iso-HMs). The key idea is to replace the solid parts of SMs with proper second-level microstructures, in which the original SMs may be stiffness anisotropic but the designed HMs have isotropic stiffness. Two classes of SMs are considered, including the microstructures with rectangular central holes and the Vidergauze-type microstructures. A parameter-sweeping design process is performed to determine the correct parameters of the employed second-level microstructures. The designed Iso-HMs are also 3D printed, where the size ratio between the specimens and the minimal feature reaches 400:1. Both numerical and experimental results validate the (nearly-)isotropic stiffness of the designed Iso-HMs with almost equal uniaxial stiffness along various directions. Furthermore, a microstructural instability analysis is carried out to investigate the buckling characteristics of Iso-HMs. The results show that the Iso-HMs are able to gain much higher buckling strength than their counterpart SMs for both uniaxial and bi-axial compressive stress loadings.

In the following, the modeling and design approaches of Iso-HMs are illustrated in section 2. The numerical results of the stiffness and buckling strength are presented and discussed in section 3, and the testing results in experiments are presented in section 4. Based on the design method and results, several discussions are made in section 5. A brief conclusion is given in the final section.

## 2. Design methods

This study aims to design HMs with isotropic elastic stiffness, and then examine their failure strength when buckling instability is triggered. The Iso-HMs are designed based on the SMs which originally have orthotropic stiffness. This section will illustrate the modeling and design approach of Iso-HMs.

### 2.1. Modelling of HMs and mechanics principles

The HMs are modeled by replacing the solid parts of prescribed SMs with arrayed second-level microstructures, as illustrated in Fig. 1. For a given SM, an arrayed second-level microstructure is employed for modeling HMs, where the size of the second-level unit cell is much smaller than that of the SM cell (Fig. 1a). A Boolean intersection is then conducted, where the overlapping domains between the solid parts of the SM (i.e. the members of the SM) and the second-level microstructure are reserved and other parts are removed (Fig. 1b). The obtained microstructure is regarded as an HM, where hierarchy arises in the sense that the microstructure comprises hierarchical members which are comprised of arrayed struts in the second level, as shown in Fig. 1c. The reserved domains are denoted by the second-level struts in the below. Because the considered SMs have plane geometric symmetries (as seen from Fig. 3a and 3b), this intersection process is firstly conducted in the top-right quarter domain of the unit cell and then the quarter domain is mirrored twice with respect to the $\times$ and $y$ axes to obtain a full HM unit cell (Fig. 1c). Such a building process ensures a plane symmetry and periodicity of the obtained HM cell. The relative density is defined as the volume fraction of the reserved second-level struts in the HM unit cell, which is denoted by $\rho$. Finally, the HM unit cell is repeated along two periodic directions to generate the full HM material (Fig. 1d).

It is known that the effective stiffness of a microstructure is determined by its deformations subjected to macroscopic stress/strain loadings (see Eq. (A2) in Appendix A). Accordingly, the effective stiffness of the HM is determined by the co-deformations of the members in two levels, which is essentially different from SMs whose stiffness is determined by the co-deformations of the members in a single level. In this way, the HMs can undergo richer deformation modes than SMs by using various second-level microstructures. An example is illustrated in Fig. 2. When a biaxial compressive stress is applied, the SM can undergo a unique deformation mode. For comparison, various deformation modes are triggered in the HMs which are highly affected by the orientations and widths of the second-level struts (Fig. 2a). On this basis, these HMs provide various types of stiffness variations along different directions (Fig. 2b). In this way, it is possible to obtain HMs with isotropic stiffness by identifying proper second-level microstructures and determining correct strut orientations and widths.

### 2.2. Considered SMs and second-level microstructures

In this study, two classes of 2D SMs are considered, as their geometries shown in Fig. 3. The first class of SMs includes a rectangular hole in the center of a square unit cell, where the hole size along the $y$-axis is $R_H$ times of that along the $x$-axis (Fig. 3a). Their effective stiffness are typically orthotropic since they possess plane symmetries. The polar chart of one such SM is illustrated in Fig. 3a, where $E^H(\theta)$ indicates the uniaxial stiffness along the direction with an angle $\theta$ to the $x$-axis, with $\theta$ sweeping from 0° to 360°. Closely related to the SM geometries, the variation of $E^H(\theta)$ also meets a plane symmetry, where two local maximal $E^H(\theta)$ are along the $x$- and $y$-axes and one minimal $E^H(\theta)$ is lying in-between. The ratios between the two maximal $E^H(\theta)$, the ratios between the minimal and maximal $E^H(\theta)$, and the directions of the minimal $E^H(\theta)$ all rely on the hole sizes. It has been demonstrated that this family of SMs is capable of attaining optimal stiffness in theory for any single stress loadings [48]. In the special case of $R_H = 1$, the SMs include square central holes and meet 1/8 geometric symmetries, therefore becoming cubic materials. They have two equal maximal $E^H(\theta)$ and the minimal $E^H(\theta)$ is lying along body diagonals. They are able to attain the maximal bulk modulus in theory, but the corresponding shear modulus is relatively small. It is noted that this class of SMs cannot obtain isotropic stiffness for any hole size.

The other class of SMs is referred to the Vidergauze-type microstructures. Therein, one unit cell is comprised of three sets of equally-sized struts in triangular patterns and the cell meets at least a plane geometric symmetry (Fig. 3b). The ratio of the cell length along the $x$-axis to that along the $y$-axis is denoted by $R_{cell}$, which can be varied and determines the directions of struts. These SMs are orthotropic and their stiffness variations meet plane symmetries (see the illustrative polar chart in Fig. 3b). Moreover, the ratio between the maximal and minimal uniaxial stiffness decreases as $R_{cell}$ increases. When it reaches $R_{cell} = \sqrt{3}$, the SM meets a six-fold rotational symmetry, and it becomes an isotropic

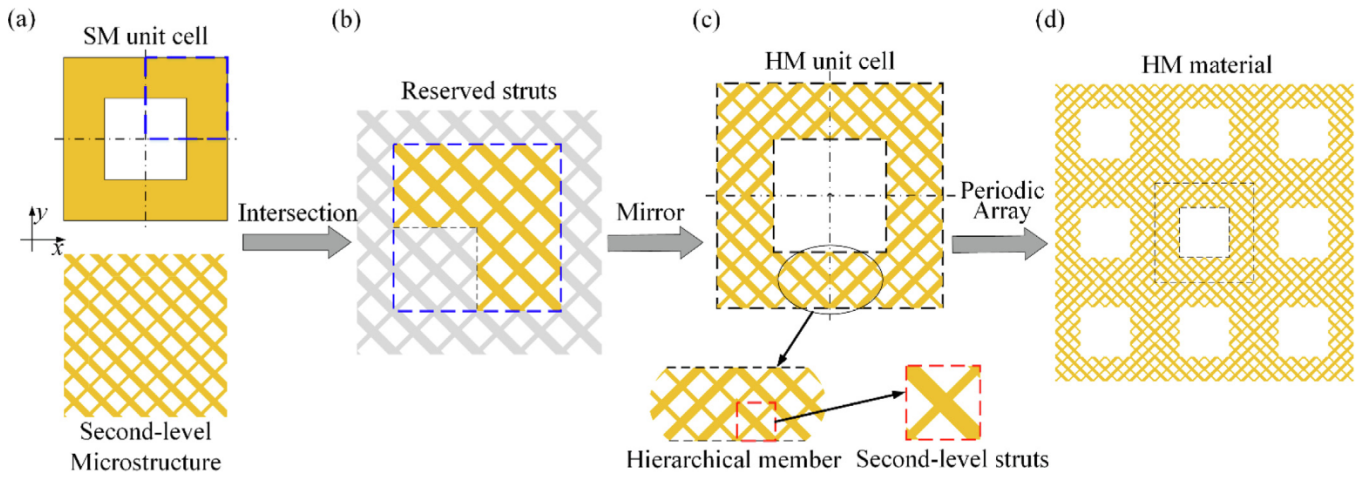


**Fig. 1.** Modeling process of an HM material. (a) A prescribed SM and a second-level microstructure; (b) a hierarchical microstructure in the quarter part of the unit cell through an intersection operation, with the reserved struts highlighted by color and the removed members by light grey; (c) a full HM unit cell after mirroring the quarter domain, which comprises the hierarchical members that are formed by arrayed second-level struts; and (d) a full HM material via a periodic array of the HM unit cell.

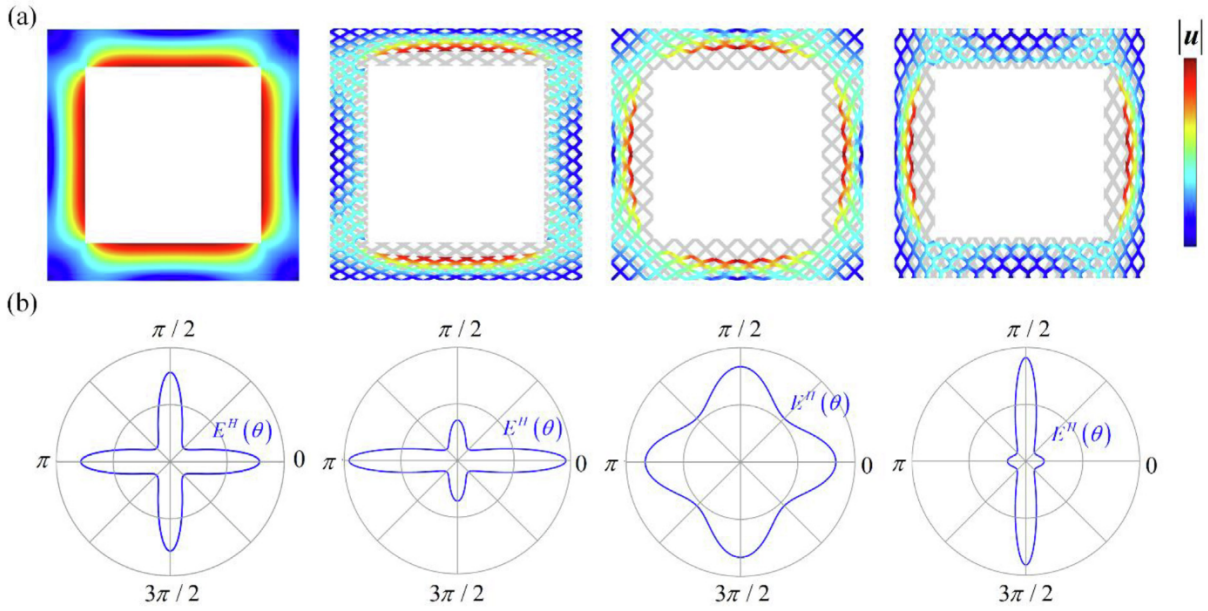


**Fig. 2.** Deformation modes and stiffness characteristics of a SM and HMs. (a) Deformation modes of the SM and HMs for bi-axial stress, where the SM undergoes a unique mode but the HMs with different second-level strut widths and orientations undergo different modes; and (b) the corresponding polar charts, indicating the variations of uniaxial stiffness along different directions. In the deformation plots, the color bar indicates the norm of displacement field $\boldsymbol{u}$, and grey shadows indicate undeformed configurations. In the polar charts, $E^H(\theta)$ is the uniaxial stiffness along the direction with an angle $\theta$ to $\times$ axis.

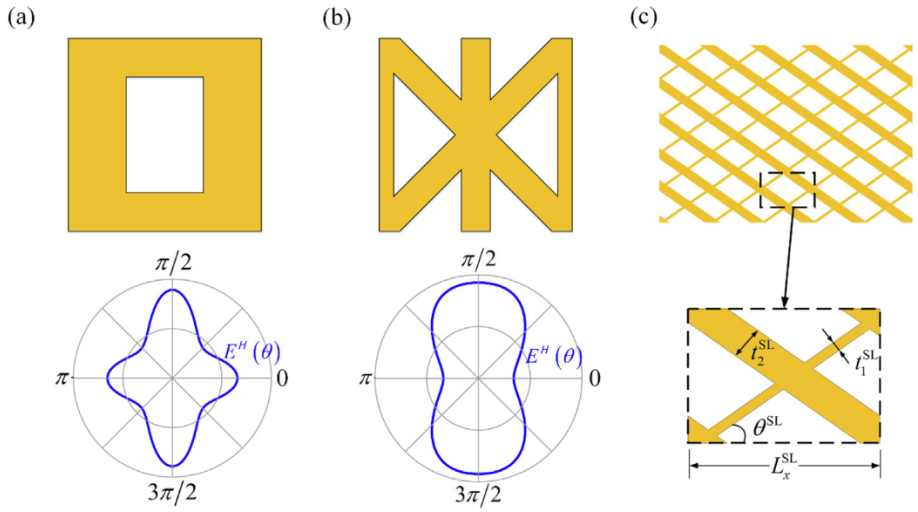


**Fig. 3.** Considered SMs and the selected second-level microstructure. (a) The SM with a rectangular central hole and its illustrative polar chart; (b) the Vidergauze-type SM and its illustrative polar chart; and (c) the selected second-level microstructure, together with the three design parameters in a unit cell.

microstructure whose polar chart is a full circle. This isotropic SM is stiffness optimal in the sense that its bulk, shear, and Young's moduli simultaneously reach the stiffness upper bound in theory (in the low density limit). Except $R_{\text{cell}} = \sqrt{3}$, the Vidergauze SMs with any other length ratios cannot obtain isotropic stiffness.

The microstructure whose single unit cell comprises two crossing struts is employed as the second-level microstructure, as illustrated in Fig. 3c. The two struts are layered along the body diagonals of the unit cell. Three parameters are used to represent their geometries, including two strut widths $t_1^{\text{SL}}$ and $t_2^{\text{SL}}$, and the inclined angle of one strut with respect to the $x$-axis, which is denoted by $\theta^{\text{SL}} \in [0 \quad 90^\circ]$. The unit cell is rectangular, where the edge length along $\times$ is denoted by $L_x^{\text{SL}}$ and the length along $y$ is obtained by $L_x^{\text{SL}} \tan\theta^{\text{SL}}$. In the design process, $L_x^{\text{SL}}$ is manually prescribed to determine the number of second-level unit cells in the HMs, where a smaller $L_x^{\text{SL}}$ usually indicates more second-level cells included. The main reason to select such second-level microstructures is their simple geometries, which makes them preferable to other candidates with more struts from a manufacturing perspective in applications. Moreover, they can provide the hierarchical members with enhanced local stiffness along different directions by tuning the orientations and widths parameters, therefore leading to various deformation modes and effective stiffness characteristics.

### 2.3. Numerical analysis

The asymptotic homogenization method is used to estimate the effective stiffness of the microstructures. This method assumes that the displacement at a macroscopic point can be expanded in

an asymptotic form, where the microscopic displacement field is periodic across unit cells. In 2D, three characterized macroscopic strains are applied to the unit cell, and periodic displacement boundary conditions are enforced. The microscopic displacement field is obtained by solving equilibrium equations (A1), and then the effective stiffness is obtained by Eq. (A2), denoted by $\boldsymbol{D}^H = D^H_{ijkl}$. More details about the theory of the asymptotic homogenization method are referred to e.g. [49] and the numerical implementation is referred to [50,51].

A parameter sweeping procedure is conducted to numerically determine the correct design parameters for realizing isotropic stiffness. For different SMs, different sets of parameters are swept. For the SMs with square holes, the orientation of the second-level struts is fixed along the body diagonals of the HM cell (i.e. $\theta^{SL} = 45°$) and the two second-level struts have equal width. Hence, only one strut width is swept. For the SMs with rectangular holes, $\theta^{SL}$ needs further to be determined since two local maximal $E^H(\theta)$ are not equal. That is, both $\theta^{SL}$ and $t_1^{SL} = t_2^{SL}$ are swept in a nested two-level loop. For the Vidergauze-type SMs, all three parameters $\theta^{SL}$, $t_1^{SL}$ and $t_2^{SL}$ are swept in a nested three-level loop.

Because all the considered SMs and HMs are orthotropic, the coupling entries in $\boldsymbol{D}^H$ that relate normal/shear strains to shear/normal stresses must be zeros, i.e. $D^H_{1112} = D^H_{2212} = 0$. An index which is stated in terms of the other entries is adopted to measure the anisotropic order of the effective stiffness of the microstructures, which is $Z = \left[\left(D^H_{1111} - D^H_{2222}\right)^2 + \left(D^H_{1111} - D^H_{1122} - 2D^H_{1212}\right)^2\right] / \left(D^H_{1111}\right)^2$. This index has been widely used in the area of structural optimization for ensuring an isotropic design [21,52], although other indices can be applied, such as the universal anisotropy index [53]. A fully isotropic microstructure is identified by $Z = 0$, while a larger $Z > 0$ indicates a higher anisotropic order of the effective stiffness. Moreover, the effective modulus can also be evaluated from $\boldsymbol{D}^H$. The uniaxial stiffness along $\theta$ is evaluated by $E^H(\theta) = 1/C^H_{1111}(\theta)$, where $\boldsymbol{C}^H(\theta) = \left(\boldsymbol{D}^H(\theta)\right)^{-1}$ is the compliance tensor based on the rotated stiffness tensor $D^H_{ijkl}(\theta) = T_{ijpq}(\theta) D^H_{pqmn} T_{klmn}$, with $T_{ijkl}$ for the transformation tensor. For an isotropic microstructure, the uniaxial stiffness is equal along all directions which is denoted by $E^H_{iso}$. The bulk modulus and shear modulus are evaluated by $K^H = \left(D^H_{1111} + D^H_{2222} + 2D^H_{1122}\right)/4$ and $G^H = 1/C^H_{1212}$, respectively. There, $K^H$ is invariant to $\theta$ and $G^H$ is estimated for $\theta^{SL} = 0°$.

Because the second-level microstructure is cut off by the interior boundaries in the unit cell, over-hanged second-level struts may be created in the HMs (Fig. 4a). They do not contribute to the effective stiffness as they are not well connected, but they cost material usage. The effective stiffness of such HMs does not vary continuously to relative densities, where the HMs may have almost the same stiffness under various $\rho$ and suffer from a sudden change of stiffness once the struts are connected again (Fig. 4a). To address this issue, a uniform layer of solid frames is attached surrounding the interior boundaries of the SMs for modeling HMs (Fig. 4b). As the second-level struts are always connected to the solid frames, the HMs gain continuous stiffness for varying $\rho$ (as the results shown in section 3.1). Note that the solid frames are not attached to the exterior edges of the unit cell, because for periodic unit cells, the struts in the exterior edges can always be well connected.

Besides stiffness, the buckling characteristics of the designed Iso-HMs are also analyzed. Subject to macroscopic stress $\tilde{\boldsymbol{\sigma}}$, a microstructural instability analysis is executed to identify the critical buckling mode and the critical buckling load, which is $\hat{\sigma}_{cr} = P_{cr}\left|\tilde{\boldsymbol{\sigma}}\right|$ with $P_{cr}$ for the critical eigenvalue. It is noted that periodic microstructures may be buckled either within a single unit cell or across multiple unit cells, corresponding to local and non-local buckling modes, respectively. In order to capture all possible modes, the Floquent-Bloch boundary conditions are enforced on the pairs of nodes on the opposite edges of the unit cell (see Eq. (A5)), and then the eigenvalue equation (A3) is solved by sweeping the wave vector $\boldsymbol{k}$ over the Brillouin zone. The band diagram indicating the first-order eigenvalue at each $\boldsymbol{k}$ is plotted. The minimal value in the diagram is taken as $P_{cr}$ and the real part of the corresponding eigenvector is plotted to represent the critical buckling mode. The numerical implementation of the microstructural instability is referred to [47].

### 2.4. Numerical implementation

The above design and analysis process is conducted by using COMSOL-with-Matlab. There, the commercial software COMSOL is adopted for modeling HMs, where the geometry for each set of parameters is explicitly built and meshed, and the developed in-house codes in Matlab are used for property analysis. Because all the concerned microstructures have at least 1/4 symmetries, only the top-right quarter domain of the unit cell is used for stiffness analysis, where the symmetric displacement boundary conditions are imposed on the mirrored edges of the unit cell. In the microstructural instability analysis, the entire unit cell is used and $\boldsymbol{k}$ is swept over five boundaries of the first irreducible Brillouin zone in the order $\Gamma - X - M - \Gamma - K - M$, as shown in Fig. A1. To ensure numerical accuracy, at least 6 layers of three-node triangular elements are meshed in the width direction of the second-level struts and the solid frames.

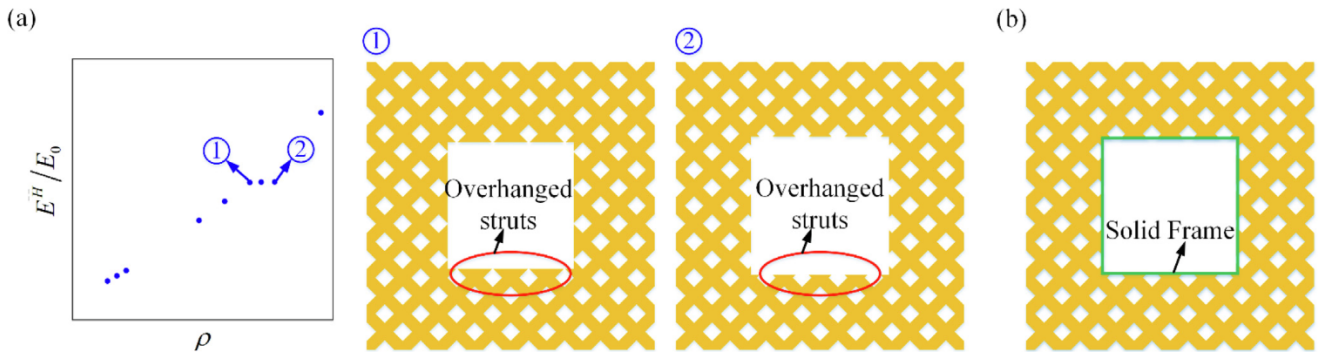


**Fig. 4.** Illustration of over-hanged struts and solid frames in HMs. (a) Two HMs with over-hanged struts, where they have the same $E^H$ at different $\rho$; and (b) the HM with a layer of solid frames.

In the numerical procedure, the best sets of widths and angles are identified by using an adaptive strategy, where the step sizes are adaptively refined in three rounds. Firstly, the widths and angles are uniformly varied with step sizes of $5L/1000$ and $0.5^\circ$, respectively. There, $L$ indicates the cell length along $\times$ axis, and the minimal and maximal thresholds for the widths and angles are $t^{SL} \in [5 \quad 85]/1000L$ and $\theta \in [10^\circ \quad 45^\circ]$. The microstructures meeting $Z < 0.1$ are identified, where the $i$th microstructure has $(t^{SL})_i^{1st}$ and $\theta_i^{1st}$. Then, additional sampling points with refined step sizes are added around these microstructures, which are at $(t^{SL})_i^{1st} \pm 2L/1000$ and $\theta_i^{1st} \pm 0.2^\circ$. In this way, two, eight and twenty-six refined sampling points are added for each microstructure for design of Iso-HMs with square holes, Iso-HMs with rectangular holes and Vidergauze Iso-HMs, because one, two and three parameters are used. The numerical procedure is re-run on the newly-added sampling points, and the microstructures satisfying $Z < 0.01$ are further identified. After that, a third round of refinement is carried out by step sizes $L/1000$ and $0.1^\circ$. Finally, the HM with minimal $Z$ is taken as the Iso-HM. Although smaller steps may yield finer results with smaller $Z$, the obtained Iso-HMs may not be able to be 3D printed because of the printing precision and resolution by the available 3D printer. Such an adaptive strategy can identify the HMs with minimal Z with high efficiency compared to the strategy by sweeping the variables with minimal step sizes over the entire parameter space.

The simulation is conducted in the plane stress condition, where the microstructures have a unit out-of-plane thickness. The 2D three-node linear triangular elements are used in the simulation, and at least six layers of elements are meshed in the width direction of the second-level struts and solid frames, which generates 200–800 thousand elements. A mesh convergence study is carried out by using different element types and different element numbers, and the results show that such a mesh implementation can guarantee a high computational accuracy (see the results and discussions in Appendix B).

## 3. Numerical results

In this section, the isotropic stiffness of the designed Iso-HMs is first verified, and then the buckling strength and modes are examined. For the microstructures with rectangular holes, square HM cells are used, and for the Vidergauze-type microstructures, rectangular HM cells are used with $R_{cell}$ = 0.8, 1, and $\sqrt{2}$. The width of the solid frame is given by $L/100$, which also determines the minimal feature size in the 3D-printed specimens (see section 4). In the numerical results, the effective stiffness and buckling strength are both regularized by the Young's modulus of the base material $E_0$. The properties of the Iso-HMs are compared with their SM counterparts, where the SMs with various $\rho$ are modeled by proportionally scaling their member sizes.

### 3.1. Isotropic stiffness of Iso-HMs

Fig. 5a presents the configurations and stiffness characteristics of the designed Iso-HMs with square holes. In the results, the length of a second-level unit cell along the $x$-axis is fixed by $L_x^{SL} = L/8$, which indicates that the quadrant part of the HM cell includes four second-level cells in the direction. As seen from the polar charts in Fig. 5b, although the SMs are cubic materials with varying $E^H(\theta)$ along different directions, the obtained HMs have uniformly equal $E^H(\theta)$ along all directions. Also, they have nearly zero $Z$ values, where the maximal value for all the testing results is $Z = 2.79 \times 10^{-4}$ (Fig. 5c). Both results validate that these HMs do attain isotropic elastic stiffness. From the modulus curves in Fig. 5c, it is seen that the Iso-HMs can cover a wide range of relative densities by varying the sizes of holes and second-level struts, from about $\rho$ = 4% to full solid (i.e. $\rho$ = 100%). In general, the second-level struts in the Iso-HMs become thicker as the hole sizes decrease, resulting in larger $\rho$. In the low density range $\rho$ < 4%, possible Iso-HMs have to be comprised of slender second-level struts with thin sizes, which may cause great difficulties for both numerical analysis and practical fabrication. If taking the width of the solid frames as the minimal feature size in 3D printing, the Iso-HMs with $\rho$ > 14% are suggested for high-quality printing since the sizes of the second-level struts are bigger than that of the solid frames.

The effective Young's, bulk, and shear moduli of the obtained Iso-HMs with respect to varying $\rho$ are presented in Fig. 5c. Therein, the Iso-HMs with different $\rho$ are obtained by varying the sizes of central holes, and for each hole size, the one with minimal $Z$ is taken as the isotropic design. It is noted that varying the strut widths with the minimal step size typically causes larger density variations for the microstructures in low $\rho$ than those in high $\rho$, because the microstructures in low densities comprise thin-sized struts. As a result, more dispersed scattered data points could be obtained in low densities.

It is observed that over the entire density range, $E_{iso}^H$ of the Iso-HMs are smaller than the maximal $E^H(\theta)$ of the SMs but larger than the minimal $E^H(\theta)$, which are along axial and body diagonals, respectively (also see the polar charts in Fig. 5b). Even for the SMs with a remarkably large difference between the maximal and minimal $E^H(\theta)$ (such as the case of $\rho$ = 13.96%), isotropic stiffness can also be attained. The underlying mechanics is that the second-level struts enhance the local stiffness of the hierarchical members along body diagonals (i.e. $\theta = 45°$), and thus the HMs gain improved effective stiffness in the directions compared to the SMs. Conversely, since the HMs are composed of a smaller portion of base materials in the axial directions (i.e. $\theta = 0°$ and $\theta = 90°$) than the SMs, they have decreased uniaxial stiffness. In this way, isotropic stiffness is obtained in the condition of $E(0^\circ) = E(45^\circ)$ by tuning the sizes of the second-level struts. However, as the decrease of $E(0^\circ)$ is higher than the increase of $E(45^\circ)$, the Iso-HMs have smaller bulk moduli than the SMs (Fig. 5c). In contrast, because of the inclined second-level struts and enlarged crossing sections of the hierarchical members, the Iso-HMs have enhanced capabilities to bear shear stress loadings compared to the SMs. Hence, they possess higher shear moduli than SMs (Fig. 5c).

The designed Iso-HMs with rectangular holes are presented in Fig. 6, where the SMs with various $\rho$ are obtained by tuning the hole sizes with a fixed length ratio $R_H$ = 1.5. Because the SMs with rectangular holes have larger local maximal $E^H(\theta)$ along the $y$-axis than that along the $x$-axis, the second-level struts in HMs are rotated away from body diagonals with $\theta < 45°$ for realizing isotropy. In this case, the second-level cells are rectangular, and they might be cut off by the edges of the HM cell by parts (see configurations in Fig. 6a). The sizes and orientations of the second-level struts rely on the hole sizes. Both circular polar charts and nearly-zero $Z$ values (Fig. 6b) verify that the obtained HMs are stiffness isotropic. Again, $E_{iso}^H$ of the Iso-HMs are between the maximal and minimal $E^H(\theta)$ of the SMs. It is worth noting that the obtained Iso-HMs are able to reach low densities that the SMs cannot reach (Fig. 6b). The minimal $\rho$ for the Iso-HMs is about $\rho$ = 5.68%, but that for the SMs is about $\rho$ = 34% which arises as the hole length along the $y$-axis is equal to the cell length.

The designed Iso-HMs based on the Vidergauze-type SMs are presented in Fig. 7. Three length ratios of SM unit cells are considered for design, including$R_{cell}$ = 0.8, 1, and $\sqrt{2}$. In all three cases, the quadrant domain of an HM cell includes four second-level cells along the $x$-axis, where $L_x^{SL}$ is varied accordingly. All the single-

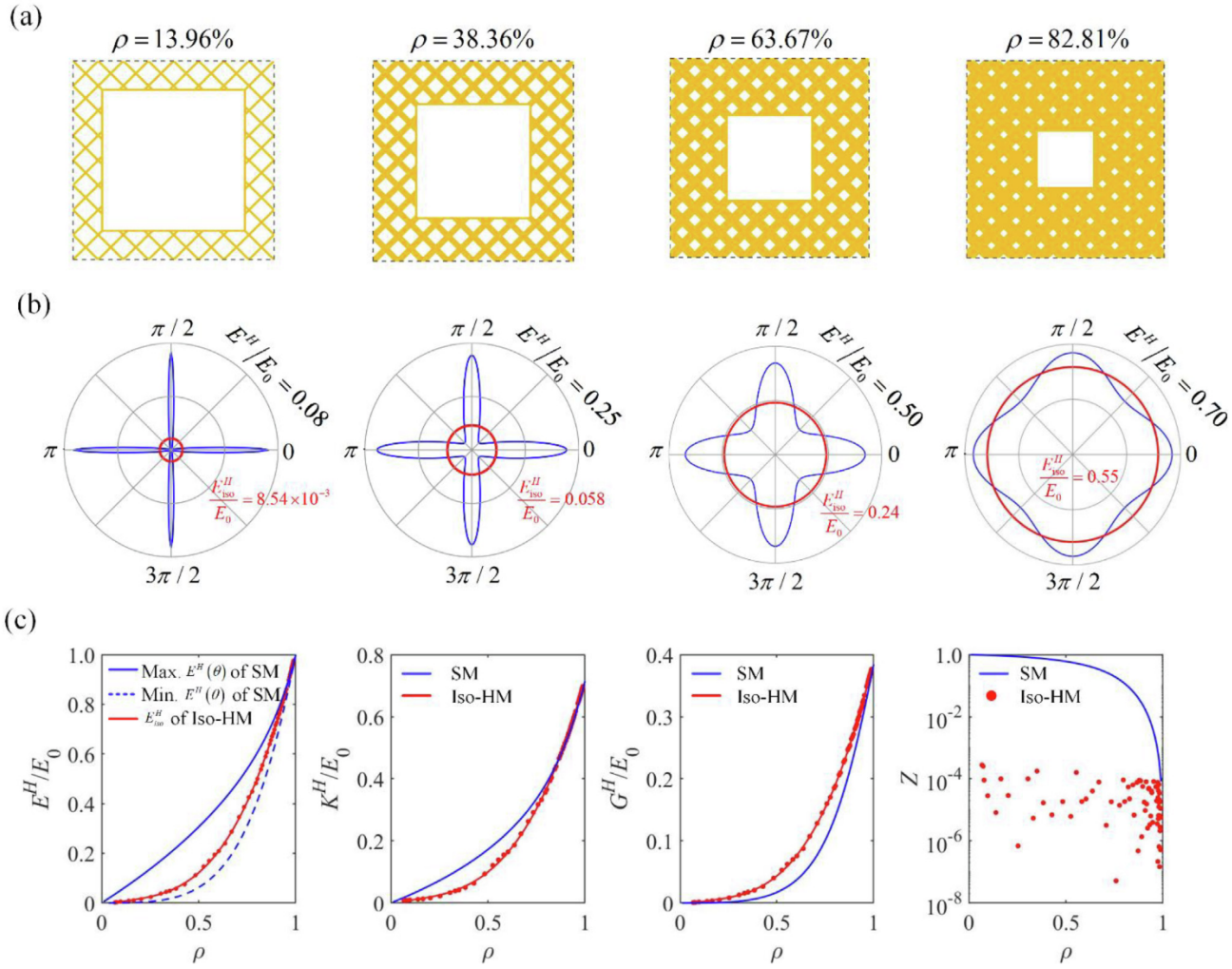


**Fig. 5.** Configurations and stiffness of the Iso-HMs with square holes. (a) Geometries of four Iso-HMs with various $\rho$, where from left to right, the hole sizes are 0.70$L$, 0.56$L$, 0.42$L$ and 0.28$L$, and the sizes of second-level struts are 0.011$L$, 0.029$L$, 0.046$L$ and 0.06$L$; (b) the polar charts of the Iso-HMs and the counterpart SMs with the same $\rho$, where the red and blue curves are for Iso-HMs and SMs, respectively; and (c) variations of uniaxial stiffness, bulk and shear modulus to $\rho$, and also the $Z$ values for SMs and Iso-HMs. (For interpretation of the references to color in this figure legend, the reader is referred to the web version of this article.)

scale members in the SMs have identical widths, and the SMs with various $\rho$ are obtained by tuning the member widths. The designed HMs can attain isotropic stiffness for any tested $R_{\text{cell}}$, although the counterpart SMs are orthotropic. In these Iso-HMs, the second-level cells are rectangular with $\theta \neq 45^{\circ}$, and the two sets of second-level struts have different widths. The orientations and widths of the second-level struts rely on $R_{\text{cell}}$ of the HM cells. In all the cases, $E^H_{\text{iso}}$ of the Iso-HMs are smaller than $E^H(\theta)$ of the SMs along all directions, and the difference between $E^H_{\text{iso}}$ and the minimal $E^H(\theta)$ of the SMs (the uniaxial stiffness along the $x$-axis) becomes larger as $R_{\text{cell}}$ increases. Also, this leads to decreased $K^H_{\text{iso}}$ and $G^H_{\text{iso}}$ compared to the SMs. In order to obtain Iso-HMs with improved stiffness, other candidate second-level microstructures with more than two sets of struts could be used, such as the ones comprising triangular-type struts.

In the same $\rho$, the HM solutions that can realize isotropic stiffness are non-unique in the sense that the Iso-HMs with different configurations can be obtained. The non-uniqueness mainly arises from two aspects. One is that the Iso-HMs may be comprised of a various number of second-level microstructures by tuning $L^{\text{SL}}_x$. An example is presented in Fig. 8a, in which three Iso-HMs comprised of 3, 5, and 6 s-level cells along the $x$-axis in the quadrant part of the HM cell are designed. Although they have the same-sized square holes and almost the same density around $\rho$ = 53%, they show quite different configurations with different sizes and arrayed patterns of second-level struts. Interestingly, despite different geometries, the three types of Iso-HMs have almost the same $E^H_{\text{iso}}$ over the entire density range and their stiffness curves almost coincide with each other (see the stiffness curves in Fig. 8a). The non-uniqueness is also attributed to the length ratios of central holes. Fig. 8b presents the designed Iso-HMs including rectangular holes with different $R_{\text{H}}$, which have different orientations and widths of second-level struts. As seen from the polar charts, each Iso-HM has a uniform isotropic stiffness along all directions, but $E^H_{\text{iso}}$ of different Iso-HMs could be different in the same density. It is noted that if the microstructures have fixed length ratios of the rectangular holes, the distinct one with minimal $Z$ among all feasible solutions with different widths and angles is taken as the isotropic design.

### 3.2. Results for buckling strength

The buckling characteristics of the designed Iso-HMs are analyzed and compared to their counterpart SMs. Only the in-plane buckling characteristics are examined in the plane stress condition,

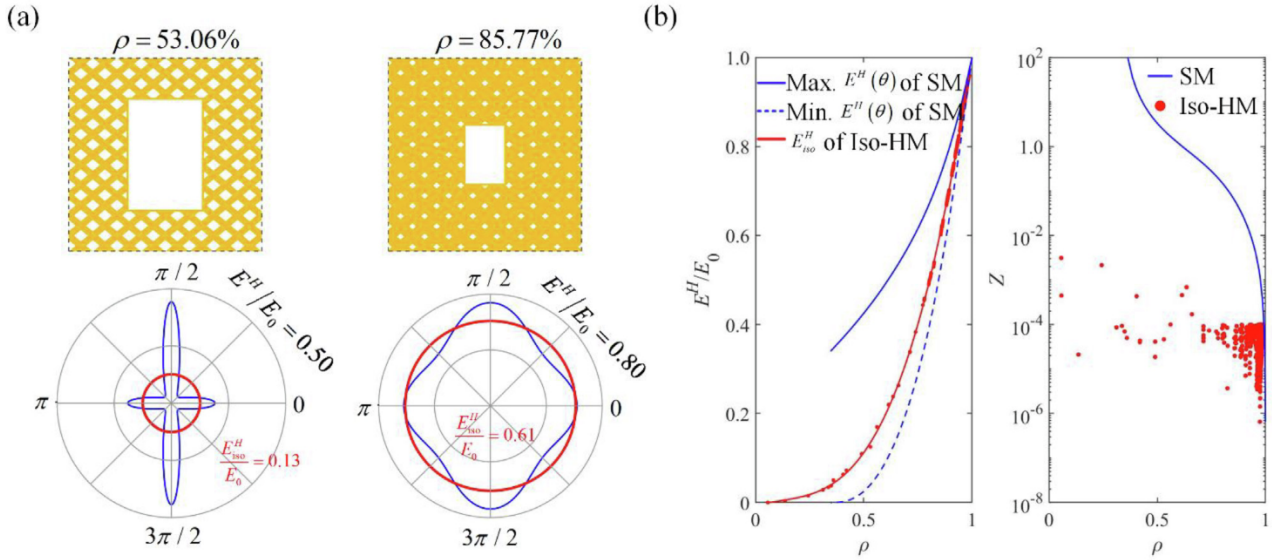


**Fig. 6.** Configurations and stiffness of Iso-HMs with rectangular holes and $R_H$ = 1.5. (a) Geometries of two Iso-HMs with various $\rho$ and their polar charts, where for the left and right Iso-HMs, their hole sizes along the $x$-axis are 0.38$L$ and 0.20$L$, sizes of the second-level struts are 0.034$L$ and 0.057$L$, and orientations of the second-level struts are 40°and 40.3°; and (b) variations of uniaxial stiffness and $Z$ values with respect to $\rho$.

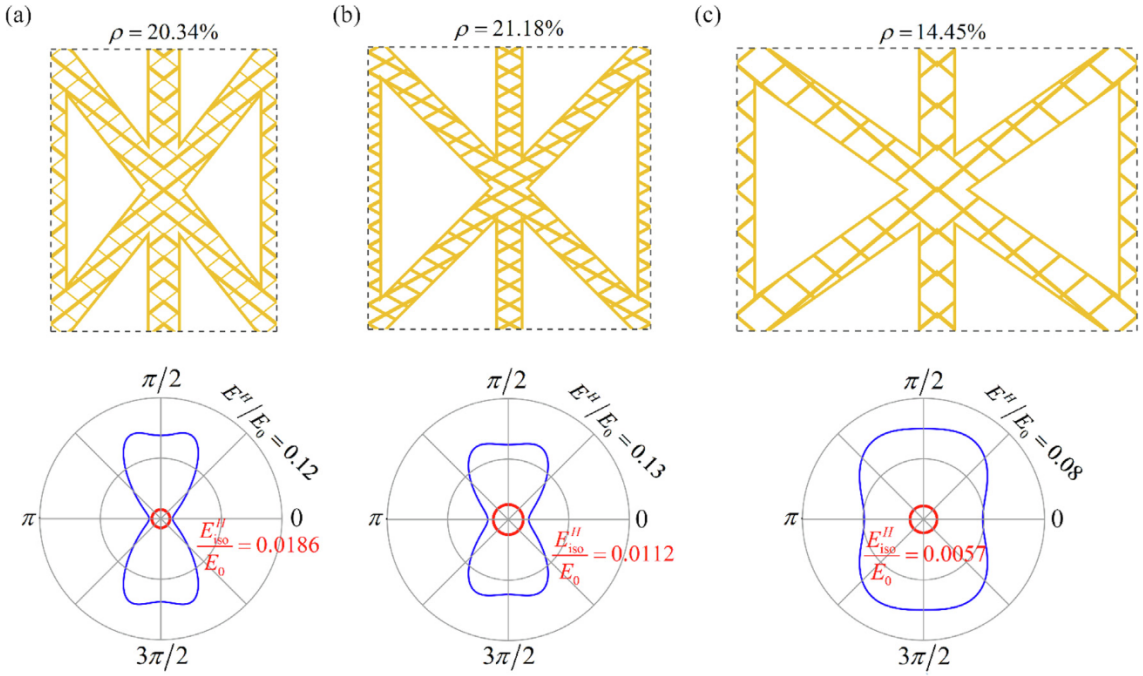


**Fig. 7.** Configurations and polar charts of Vidergauze Iso-HMs. The geometric parameters are (a) $R_{cell}$ = 0.8, $t_1^{SL} = 1.3$, $t_2^{SL} = 0.5$, $\theta^{SL} = 38.3^\circ$; (b) $R_{cell} = 1$, $t_1^{SL} = 1.3$, $t_2^{SL} = 1.1$, $\theta^{SL} = 28.8^\circ$; and (c) $R_{cell} = \sqrt{2}$, $t_1^{SL} = 1.4$, $t_2^{SL} = 1.2$, $\theta^{SL} = 40.0^\circ$. In the polar charts, the red and blue curves are for Iso-HMs and SMs. (For interpretation of the references to color in this figure legend, the reader is referred to the web version of this article.)

while the out-of-plane buckling is omitted. Fig. 9 presents the band diagrams and critical buckling modes of the Iso-HMs with square holes when they are subjected to uniaxial compressive stress $\tilde{\boldsymbol{\sigma}} = [-1 \quad 0 \quad 0]^T$. It is found that the SMs are buckled in shear modes with a long wavelength, where the modes span over all the unit cells and the critical strength are near Γ (Fig. 9a, 9c, and 9d). Differently, three types of critical buckling modes are observed in the designed Iso-HMs, which are relevant to the width of solid frames and second-level struts under various $\rho$. In the cases where the Iso-HMs are comprised of thin-sized second-level struts in low $\rho$, the critical modes are dominated by the localized buckling of the second-level struts (Fig. 9c). In contrast, the critical modes are switched to the localized buckling of the solid frames in high $\rho$, where the solid frames become the thinnest struts in the cell (Fig. 9d). In both cases, the critical modes are triggered within single unit cells and thus they are periodic across cells. Moreover, the profiles of buckled struts match well with the critical mode of a single column constrained by elastic boundary conditions, and hence the effective failure strength could be estimated simply by using semi-analytical methods [54,55]. For comparison, when the

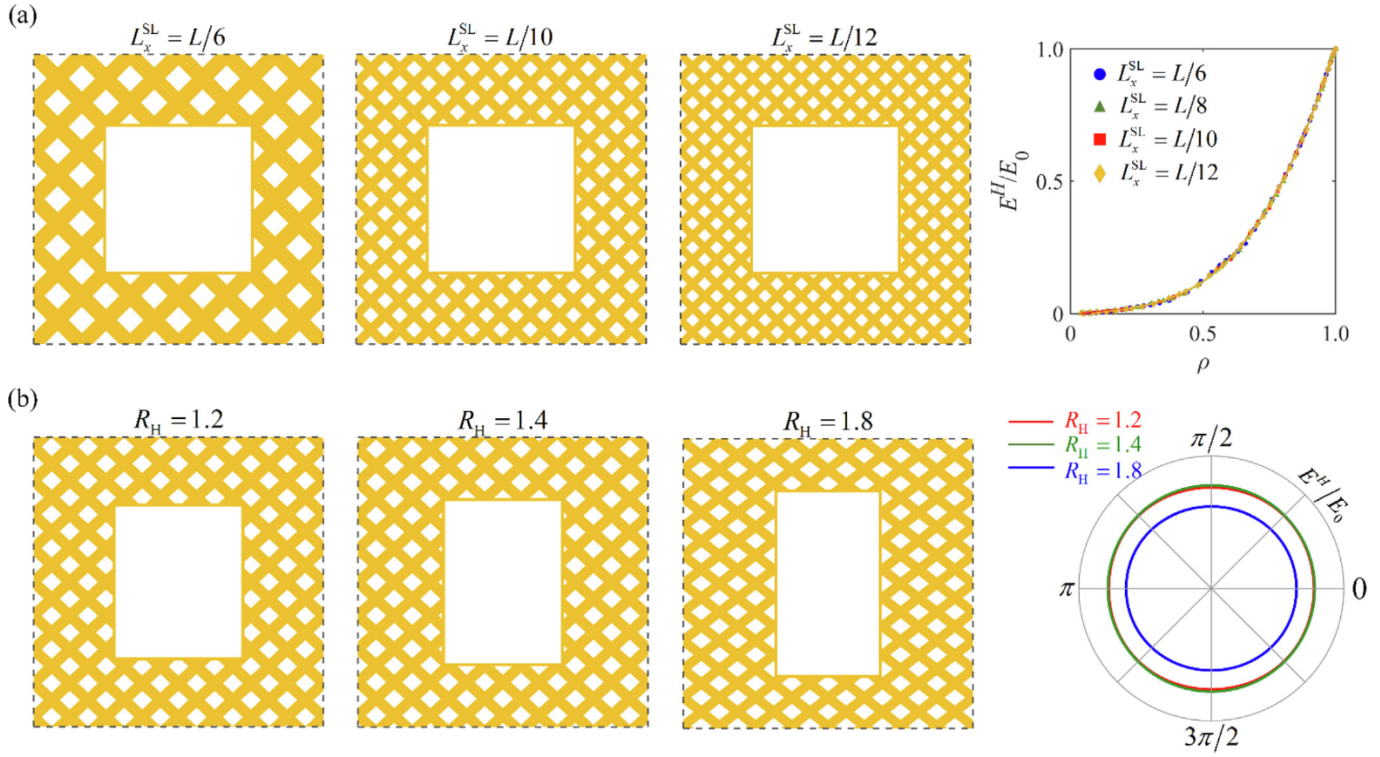


**Fig. 8.** Non-uniqueness of Iso-HMs. (a) Iso-HMs with a different number of second-level microstructures and Young's modulus of different designs to varying $\rho$, where the second-level struts have widths 0.053$L$, 0.031$L$ and 0.026$L$ from left to right; and (b) Iso-HMs with various $R_H$ and their polar charts.

widths of the second-level struts are close to those of the solid frames, the Iso-HMs suffer from non-local anti-modes along the $x$-axis. In that case, the buckling modes are repeated every two unit cells along the $x$-axis, but are periodic along the $y$-axis (Fig. 9b). In this case, the critical strength in the band diagram is at X (Fig. 9b).

A quantitative comparison of the buckling strength between the Iso-HMs and SMs is made, as shown in the diagrams in Fig. 9. The buckling strength is given in Table 1. It is observed that the band curves of the Iso-HMs have minor variations but those of SMs exhibit large variations with single dominated buckling modes. It indicates that the Iso-HMs make use of solid constituents more equally for various buckling modes than the SMs. For the Iso-HMs with $\rho$ = 7.37% and $\rho$ = 33.21%, each band curve has almost identical $P$ through all $\boldsymbol{k}$, which corresponds to the localized modes on the second-level struts and the solid frames at different positions, respectively. For the Iso-HM with $\rho$ = 20.31%, a relatively large variation is obtained, but it is still much smaller than that of the SM. By identifying the minima in the band diagrams, the Iso-HMs provide a significant increase in buckling strength in low densities. For the Iso-HM with $\rho$ = 7.37% and $\rho$ = 20.31%, the improvement of their buckling strength compared to the counterpart SMs reach 171% and 87%, respectively. The superior strength characteristics are mainly attributed to hierarchical and isotropic-stiffness design, which provides increased local stiffness along body diagonals, and thus the Iso-HMs gain improved capabilities to bear global shear buckling failure. In high densities, the Iso-HMs obtain lower buckling strength than the corresponding SMs, since the solid frames in Iso-HMs are too thin to be prone to buckle.

The buckling characteristics of the Iso-HMs and the SMs with square holes are also examined for bi-axial compressive stress $\widetilde{\boldsymbol{\sigma}} = [-1 \quad -1 \quad 0]^T$. The buckling modes and strength are presented in Fig. 10 and Table 1. The same conclusion as above can be made, where the SMs are buckled in global shear modes while the Iso-HMs are buckled in either localized modes or non-local anti-modes. For $\rho$ = 7.37% and $\rho$ = 20.31%, the buckling strength of the Iso-HMs are 55% and 71% higher than that of SMs, respectively.

The buckling performance for the microstructures with rectangular holes are compared in Fig. C1, Fig. C2 and Table 1. Again, the SMs are buckled in global shear modes and the Iso-HMs are buckled mainly in localized modes and non-local anti-modes. However, as the SMs involve thinner horizontal members than the vertical members, they become prone to suffer from buckling failure, resulting in lower buckling strength than the Iso-HMs for all the tested $\rho$. In the extreme case $\rho$ = 35.99% where the SM includes slender horizontal members, the buckling strength of the Iso-HM is a hundred times higher than those of the SMs.

The buckling characteristics of the Vidergauze-type microstructures with $R_{cell} = 1$ are presented in Fig. 11 and Table 1. For both uniaxial and bi-axial compressive stresses, this class of SMs is mainly buckled in bending modes on the strut member, which is attributed to the rigid triangular connections between different members. The buckling modes of the struts meet a rotational pattern around the member joints. The localized buckling modes can also be found in the Iso-HMs. There, the inclined hierarchical members are buckled for the uniaxial stress, while a local rotational mode near the joints is observed for the uniaxial and bi-axial stresses, respectively. From the band diagrams, it is seen that the Iso-HMs have higher buckling strength than the SMs at each $\boldsymbol{k}$, even though they have decreased stiffness. For the critical buckling strength, the Iso-HMs outperform the SMs by over 100%.

## 4. 3D printing and experimental testing

The designed Iso-HMs with square holes were 3D printed for experimentally testing isotropic stiffness. Considering the large size difference between the second-level struts and the HM cells, the 3D printer microArch S240 was used for manufacturing, allow-

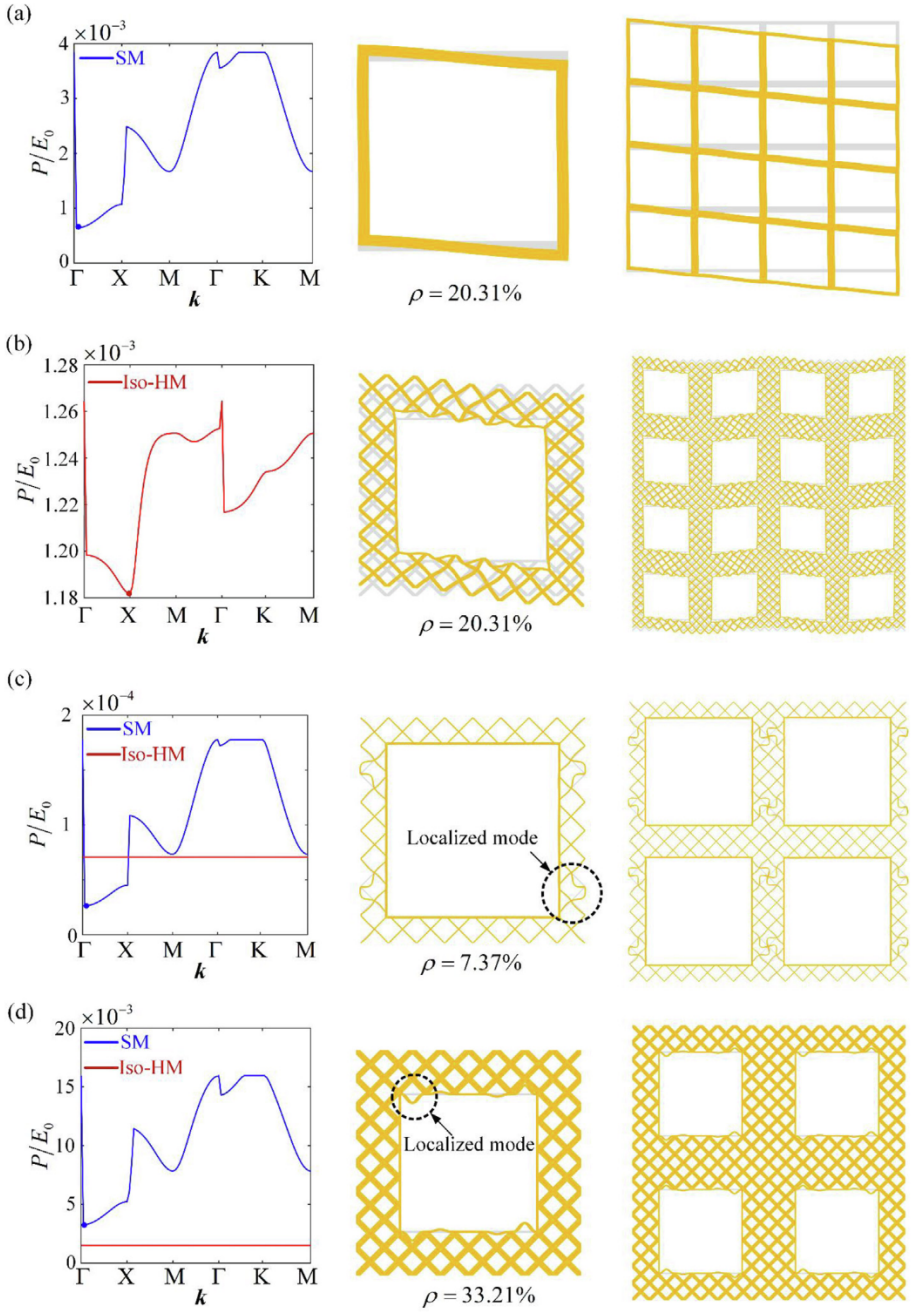


**Fig. 9.** Buckling characteristics of the Iso-HMs and SMs with square holes subjected to $\tilde{\boldsymbol{\sigma}} = [-1 \quad 0 \quad 0]^T$, for (a) the SM with $\rho = 20.31\%$ and (b)-(d) the Iso-HMs with various $\rho$. In each subplot, the left column shows the band diagrams, and the middle and right columns show the buckling modes in unit cells and arrayed cells, respectively. Grey shadows and colored regions indicate the initial and buckled states, respectively. In (a) and (b), 4-by-4 cells are used to illustrate the non-local buckling modes, while 2-by-2 cells are used to highlight the local buckling modes in (c) and (d).

ing for rapid photopolymerization of an entire layer of liquid polymer using a flash of UV light based on the technology Projection Micro Stereolithography. The HTL resin (type of Yellow-20) was used as the base material for 3D printing Iso-HMs, with Poisson's ratio of approximately 0.3. Its compression stiffness was measured by carrying out compressive testing on the square prism specimens (as seen in Appendix D), which was obtained as $E_0 = 2.19$ GPa. During 3D printing, the exposure time and light intensity were adaptively manipulated from 3 to 1 s and from 74 to 52 mW/cm$^2$, respectively. Each printing layer was 20 μm. After 3D printing, the specimens were put into a UV curing chamber for 3.5 min to cure specimens for enhanced durability and precision.

Two specimens were 3D printed, where they included 0° and 45° unit cells for testing the corresponding uniaxial stiffness. The two high-resolution specimens are presented in Fig. 12a and 12b. Therein, the minimal features were the solid frames, which had a size of 50 μm, and the HM cell was 5 mm in length. Correspondingly, the 0° specimen had an edge size of 20 mm and the 45° specimen had an edge size of $20\sqrt{2}$ mm, both including at least 4-by-4 HM unit cells. The size ratio between the specimen and the minimal feature reached over 400:1. In order to prevent out-of-plane buckling, the 2D Iso-HMs were uniformly extruded by a relatively large thickness of 3 mm for 3D printing. The surface quality of the 3D-printed specimens was examined by using a 3D digital micro-

**Table 1**
Comparison of buckling strength for Iso-HMs and counterpart SMs under various $\rho$, when they are subjected to uniaxial and biaxial compressive stresses.

| Configurations | Macroscopic Stress | $\rho$ | SM $P_{cr}/E_0$ | Iso-HM $P_{cr}/E_0$ | Improvement |
|---|---|---|---|---|---|
| Square holes | $\tilde{\boldsymbol{\sigma}} = [-1 \quad 0 \quad 0]^T$ (Results in Fig. 9) | 7.37% | $2.61 \times 10^{-5}$ | $7.07 \times 10^{-5}$ | 171% |
| | | 20.31% | $0.63 \times 10^{-3}$ | $1.18 \times 10^{-3}$ | 87% |
| | | 33.21% | $3.25 \times 10^{-3}$ | $1.52 \times 10^{-3}$ | −53% |
| | $\tilde{\boldsymbol{\sigma}} = [-1 \quad -1 \quad 0]^T$ (Results in Fig. 10) | 7.37% | $2.48 \times 10^{-5}$ | $3.86 \times 10^{-5}$ | 56% |
| | | 20.31% | $0.59 \times 10^{-3}$ | $1.01 \times 10^{-3}$ | 71% |
| | | 33.21% | $2.96 \times 10^{-3}$ | $1.88 \times 10^{-3}$ | −36% |
| Rectangular holes ($R_H = 1.5$) | $\tilde{\boldsymbol{\sigma}} = [-1 \quad 0 \quad 0]^T$ (Results in Fig. C1) | 35.99% | $1.53 \times 10^{-5}$ | $3.33 \times 10^{-3}$ | 21665% |
| | | 49.00% | $3.19 \times 10^{-3}$ | $1.17 \times 10^{-2}$ | 267% |
| | $\tilde{\boldsymbol{\sigma}} = [-1 \quad -1 \quad 0]^T$ (Results in Fig. C2) | 35.99% | $1.53 \times 10^{-5}$ | $3.33 \times 10^{-3}$ | 21665% |
| | | 49.00% | $3.17 \times 10^{-3}$ | $1.10 \times 10^{-2}$ | 247% |
| Vidergauze ($R_{cell} = 1$) | $\tilde{\boldsymbol{\sigma}} = [-1 \quad 0 \quad 0]^T$ (Results in Fig. 11) | 20.34% | $4.60 \times 10^{-4}$ | $10.40 \times 10^{-4}$ | 126% |
| | $\tilde{\boldsymbol{\sigma}} = [-1 \quad -1 \quad 0]^T$ (Results in Fig. 11) | 20.34% | $3.84 \times 10^{-4}$ | 7.78 × 10–4 | 103% |

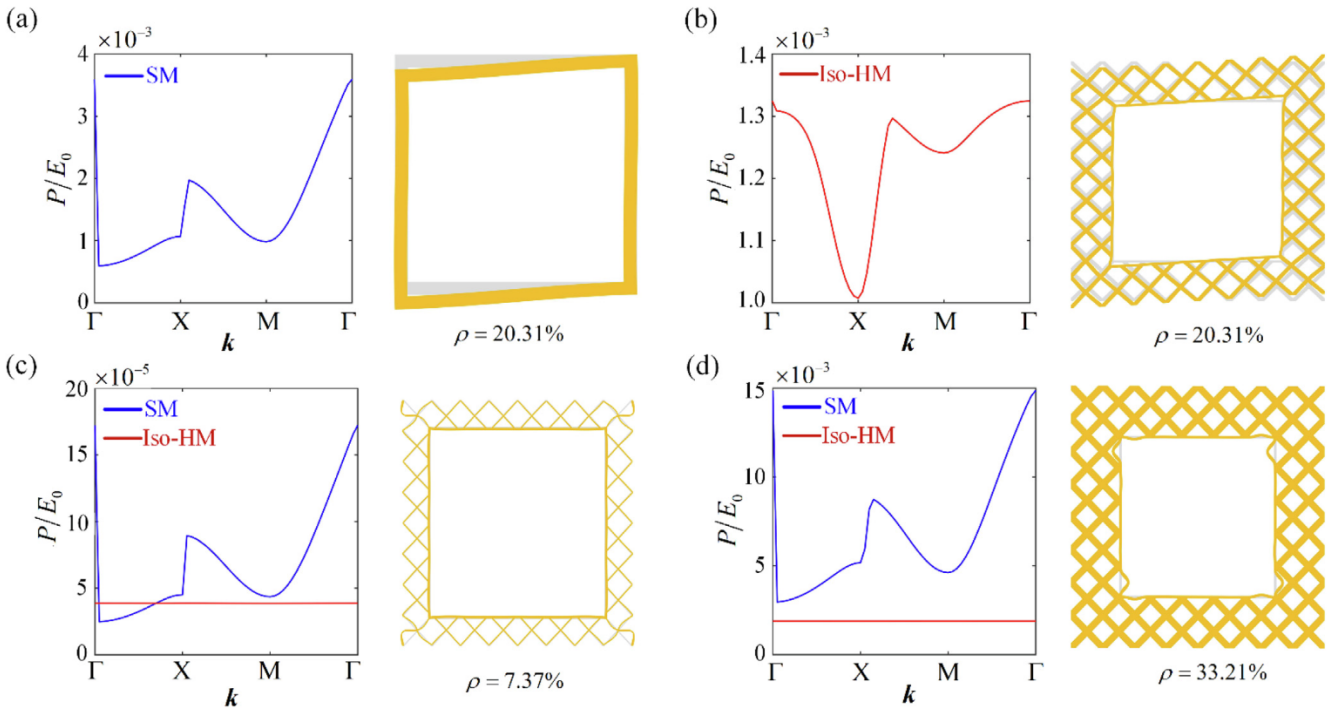


**Fig. 10.** Buckling characteristics of the Iso-HMs and SMs with square holes subjected to $\tilde{\boldsymbol{\sigma}} = [-1 \quad -1 \quad 0]^T$, for (a) the SM with $\rho = 20.31\%$ and (b)-(d) the Iso-HMs with various $\rho$. In each subplot, the left column shows the band diagrams, and the middle and right columns show the buckling modes in unit cells and arrayed cells, respectively. Grey shadows and colored regions indicate the initial and buckled states, respectively.

scope (type of Keyence VHX-600E). As shown in Fig. 12a, the specimens had smooth faces and the tiny voids were open from top to bottom surfaces without residual fluids. The relative densities of the Iso-HMs were estimated as the density ratios between the Iso-HM specimens and the square prism specimens, where the density for each specimen was obtained as its weight divided by its volume.

The uniaxial compression testing was conducted on an Instron universal test machine with a 2 kN load cell. The 0° and 45° specimens were both loaded by vertical compressions, which were used to obtain tested $E^H(0^\circ)$ and $E^H(45^\circ)$ (Fig. 12c). Both specimens were compressed by the load cell at a speed of 0.12 mm/min$^{-1}$, corresponding to a strain rate of $10^{-4}$ s$^{-1}$ for the 0° specimen and $0.71 \times 10^{-4}$ for the 45° specimen. This loading speed can ensure quasi-static loading conditions. To measure the uniaxial stiffness, each specimen was loaded and unloaded four times and $E_\theta$ was evaluated as the average of the slopes of the last three stress–strain unloading curves.

The testing results are presented in Fig. 12d. It is seen that the two 3D-printed specimens had close relative densities. Moreover, their unloading curves had almost the same slopes, where the relative difference between the two uniaxial stiffness was only $\left|E^H(0^\circ) - E^H(45^\circ)\right| / E^H(0^\circ) = 2.71\%$. The result indicates that the microstructure has almost the same uniaxial stiffness along 0° and 45°, thus it has nearly-isotropic stiffness. Because the HTL resin is a brittle material, the Iso-HM specimens were broken by abrupt collapse (Fig. 12e). For testing the buckling characteristics, other base materials are required.

The performance of the two 3D-printed specimens is also compared with the numerical results, as seen in Fig. 12d. The specimens had about 5% higher relative densities than the numerical models, but had 25.56% lower stiffness. The weight and property

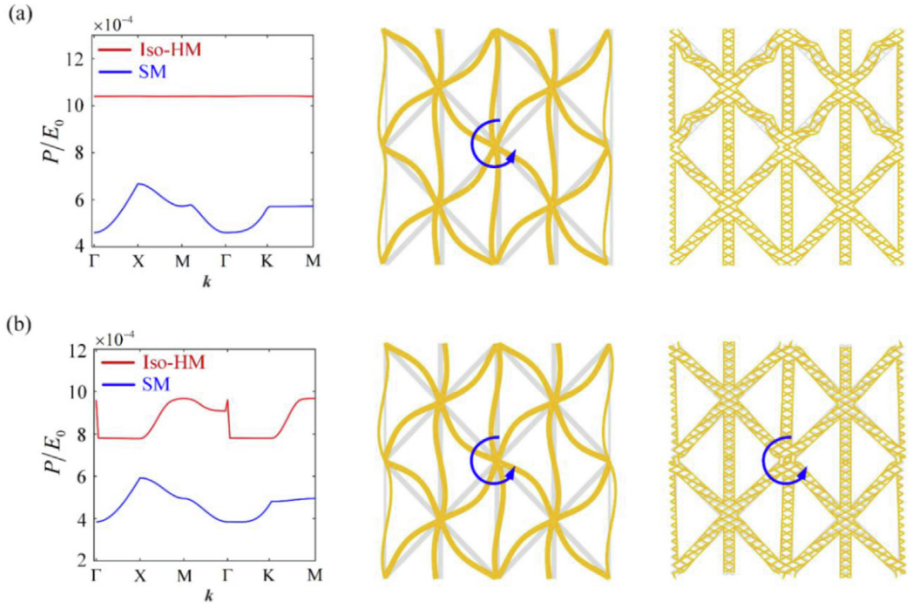


**Fig. 11.** Buckling characteristics of the Vidergauze-type Iso-HMs and SMs subjected to (a) uniaxial compressive stress $\tilde{\boldsymbol{\sigma}} = [-1 \quad 0 \quad 0]^T$ and (b) bi-axial compressive stress $\tilde{\boldsymbol{\sigma}} = [-1 \quad -1 \quad 0]^T$. In each subplot, the left column shows the band diagrams, and the middle and right columns show the buckling modes of arrayed unit cells for the SMs and Iso-HMs, respectively. The density for all the cases is $\rho = 20.34\%$. In the buckling modes, grey shadows and colored regions indicate the initial and buckled states, respectively.

differences are mainly attributed to two aspects. One is that the specimens included limited 4-by-4 unit cells, which might be insufficient for estimating the effective stiffness with high accuracy. More than four unit cells are usually required to mimic the periodic array of unit cells. The other aspect is related to the properties of the base material. As the HTL resin is viscoelastic, its density and stiffness are dependent on the loading strain rate, as well as printing parameters such as the exposure time and light intensity, and the photocuring technology may cause slight overexposure unavoidably. The properties of the base material in Appendix D are regarded as an average estimation, which may cause deviations in the properties of the Iso-HM specimens from the numerical results.

## 5. Discussions

*Differences from other studies*: Several differences from existing works can be concluded. Firstly, the design method is different. The proposed method uses a hierarchical design strategy to realize isotropy but other methods are mostly based on single-level configurations. Even in some existing studies (e.g. [34,45]), the authors mainly discussed the performance of prescribed hierarchical microstructures rather than carrying out a design process for pursuing isotropic stiffness. Secondly, the underlying mechanics to realize isotropic stiffness is different. The designed Iso-HMs attain isotropy through the co-deformations of the hierarchical members in two levels, but other existing isotropic microstructures rely on the deformations of single-level members, such as the combined microstructures [13,14] and the *n*-fold rotationally symmetric microstructures [11]. Finally, the designed Iso-HMs explore a new family of isotropic microstructures with hierarchical member features, which expand the space of already-known isotropic microstructures. To the authors' best knowledge, the hierarchical configurations have yet to be reported by other studies.

*Extensions to other anisotropic SMs*: The proposed design strategy can be extended for 3D cases. For instance, analogously to the 2D microstructures with square holes, 3D Iso-HMs could be designed by replacing the solid parts of simple-cubic SMs with body-centered-cubic second-level microstructures. For the SMs with complex geometries, both the configurations of the second-level microstructures as well as their spatial layouts in the solid parts of SMs can be taken as the design variables for a wide design space to search isotropic solutions. For a general case, the structural topology optimization method can be developed to identify proper second-level microstructures, where the isotropic stiffness is ensured by imposing a constraint in the optimization formulations. The optimized results might obtain spatially-varying second-level microstructure configurations over the solid parts of SMs. However, it is not clear if the hierarchical design strategy can be used for any kind of SMs, which deserves future research.

*Comparison to maximal stiffness in theory*: The designed Iso-HMs cannot reach the maximal stiffness in theory, which is defined by the Hashin-Shtrikman bound [11]. An example can be directly found in Fig. 6c, where the SMs with square holes attain the maximal bulk stiffness in theory (in the low density limit) but the Iso-HMs have decreased bulk modulus. As discussed in [56], the HMs with the target of maximizing both the stiffness and strength usually cannot attain the theoretical bound for elastic stiffness. Moreover, isotropy is another restriction for HMs to reach maximal stiffness. In order to identify the isotropic HMs with maximal stiffness, a structural optimization method can be used [56].

*Influence of the solid frame*: The width of the solid frame has a significant effect on the obtained configurations of the Iso-HMs. Generally, in the same density, the Iso-HMs with wider frames are comprised of thinner second-level struts. Accordingly, the Iso-HMs with different frame widths may have different stiffness. Moreover, the frame width also affects the buckling characteristics of the Iso-HMs. Because the Iso-HMs with thinner frames have to include thicker second-level struts, they are prone to be buckled on the frames, while those with wider frames are prone to be buckled on the second-level struts. It is noted that the design process may not be able to find feasible solutions in low densities if the HMs include wide frames, since too thin second-level struts are

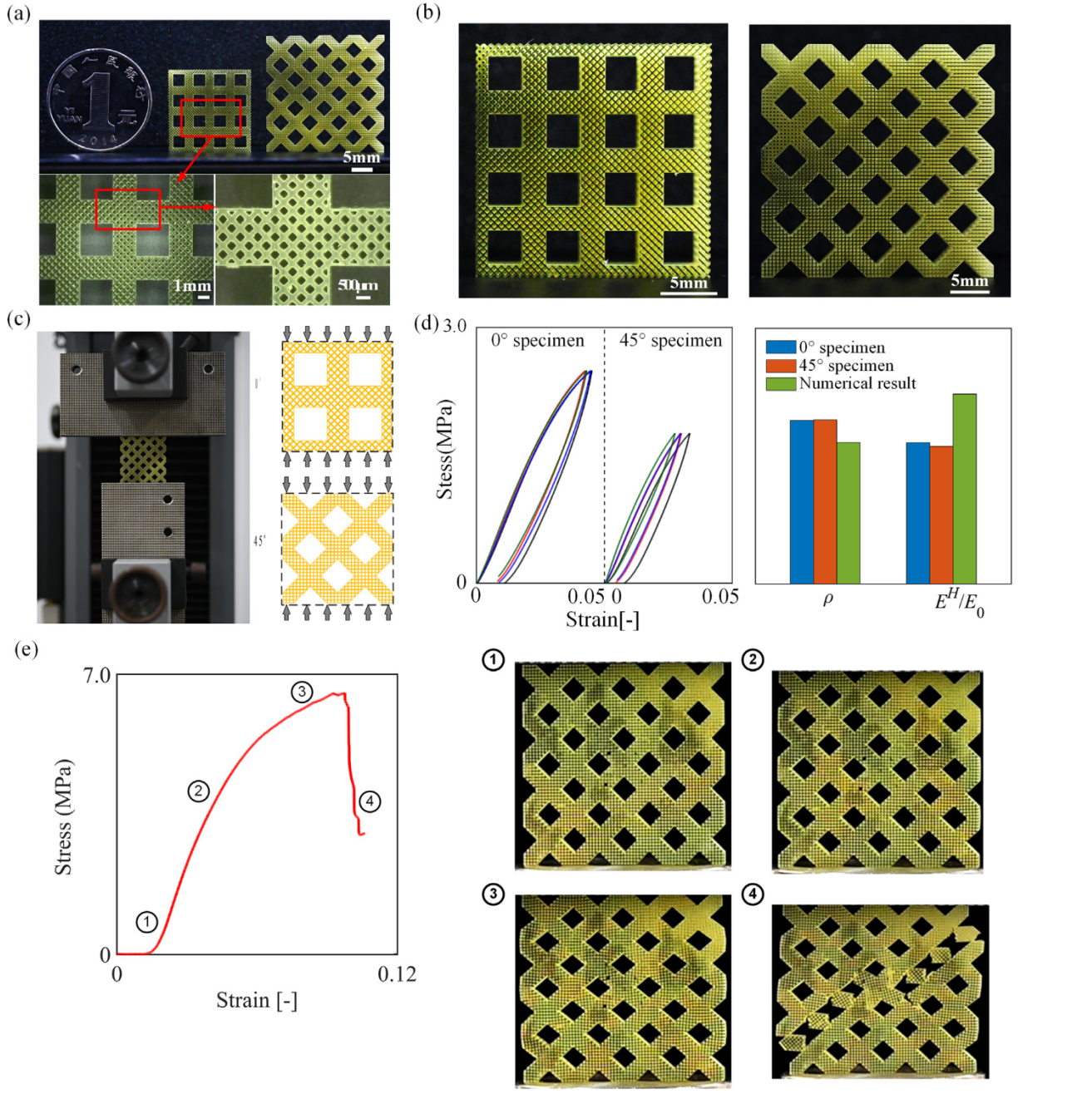


**Fig. 12.** 3D-Printed specimens and experimental testing. (a) 3D-printed specimens with magnified images showing the features in fine resolutions; (b) two specimens including $0^{\circ}$ and $45^{\circ}$ unit cells in the left and right subplots, respectively; (c) experiment set up, where two specimens were both loaded vertically; (d) testing results, where the left subplot shows the loading–unloading curves for each specimen and the right one shows the tested $\rho$ and uniaxial stiffness, together with the numerical results; and (e) broken mode of one specimen, where the left subplot shows the loading curve, and the right subplots show the compressed specimens in four stages, and the last specimen presents abrupt collapse.

required. Furthermore, the frame width affects the fabrication quality, where it has to be bigger than the minimal fabricable feature size of the available 3D printer, otherwise, manufacturing may fail.

*Other hierarchical modeling methods*: An alternative method to model hierarchical microstructures is to use body-conformal second-level microstructures, where the second-level struts are aligned with the interior boundaries of SMs. This method does not require solid frames surrounding the interior boundaries of HMs, since it does not create over-hanged second-level struts. Moreover, this modeling approach is suitable for the microstructures with complex geometries. As the body-conformal second-level struts are typically irregular, a large number of strut widths and orientations need to be determined. Also, the designed HMs are dependent on the connections and resolutions of second-level struts in the initial design. Other modeling approaches can also be developed under requirement.

## 6. Conclusions

In this paper, we propose a new class of isotropic hierarchical microstructures. Such microstructures are modeled by replacing the solid parts of SMs with second-level microstructures, resulting in hierarchical member features in two levels. Different from any existing isotropic microstructures, these Iso-HMs realize isotropy

based on the co-deformations of the members in two levels. In this way, isotropic stiffness can be obtained even for the SMs which originally have anisotropic stiffness. Two types of SMs are used for design of Iso-HMs, including the ones with rectangular holes and the Vidergauze-type SMs. Moreover, the designed Iso-HMs are 3D printed and their stiffness performance are experimentally tested, where the specimens have a length ratio between the unit cell and the minimal feature over 400:1. Both numerical and experimental results verify the isotropic stiffness of the design Iso-HMs. Moreover, a structural instability analysis is made for the Iso-HMs. Compared to single-level microstructures, the hierarchical design can significantly improve the critical buckling strength, and can also change the critical buckling modes. The hierarchical design strategy, the novel mechanics principle for realizing isotropy, and the new hierarchical configurations could be helpful for exploring a wider range of functional microstructures in various applications.

In future, other properties besides the effective stiffness and buckling strength could be designed for Iso-HMs. For instance, negative Poisson's ratios can be realized by hierarchical designs, however the method to design auxetic Iso-HMs is yet to propose. Moreover, because the HMs comprise of thin-sized second-level struts, they may also suffer from stress yielding failure. In this sense, numerical studies by incorporating both material and geometric nonlinearies could be conducted to identify the major failure modes of the Iso-HMs in different relative densities. In addition, a structural topology optimization method can be proposed to design Iso-HMs with extreme stiffness and buckling strength with respect to specific constraints, where both the configurations and spatial layout of the second-level microstructures can be automatically determined.

## Data availability

No data was used for the research described in the article.

## Declaration of Competing Interest

The authors declare that they have no known competing financial interests or personal relationships that could have appeared to influence the work reported in this paper.

## Acknowledgment

Y.Q. Wang acknowledges support from the National Natural Science Foundation of China (Grants 12172075), Liaoning Revitalization Talents Program (XLYC2007027), and Fundamental Research Funds for the Central Universities (DUT19RC(3)072). F. W. Wang acknowledges support from the Villum Fonden through the Villum Investigator Project InnoTop. The authors acknowledge Ms. Qiao Xu from the School of Mechanical Engineering, Dalian University of Technology, for her advice in experimental testing.

## Appendix A. Equations for homogenization analysis and microstructural instabilities

The effective stiffness of the microstructures is numerically calculated by using the asymptotic homogenization method. There, a unit cell is loaded by three characterized macroscopic strains $\widetilde{\varepsilon}_{ij}^{(pq)}$, where $\widetilde{\varepsilon}_{ij}^{(pq)}=1$ for $ij=pq$ and otherwise, $\widetilde{\varepsilon}_{ij}^{(pq)}=0$. The stiffness tensor of the microstructure is calculated by

$$D^H_{pqmn}=\frac{1}{V_{\text{cell}}}\int_\Omega (D_0)_{ijkl}\left(\widetilde{\varepsilon}_{ij}^{(pq)}-\varepsilon_{ij}^{(pq)}\right)\left(\widetilde{\varepsilon}_{kl}^{(mn)}-\varepsilon_{kl}^{(mn)}\right)d\Omega,\quad (i,j,k,l,p,q,m,n=1,2)$$

where $\Omega$ indicates the domain of the unit cell, $V_{\text{cell}}$ is the cell volume, $(D_0)_{ijkl}$ is the stiffness tensor for the solid constituent, $\varepsilon_{ij}^{(pq)}=\partial u_i^{(pq)}/\partial x_j$ is the obtained microscopic strain tensor, where $x_j$ is the space variable in $\Omega$ (with $j=1,2$ for $\times$ and $y$, respectively), and the microscopic displacement $u_i^{(pq)}$ is calculated by solving the equilibrium equation,

$$\int_\Omega D^s_{ijkl}\left(\widetilde{\varepsilon}_{ij}^{(pq)}-\varepsilon_{ij}^{(pq)}\right)\frac{\partial v_k^{(pq)}}{\partial x_l}d\Omega=0,\quad \forall v_k^{(pq)}\in\bar{U}\quad (i,j,k,l,p,q=1,2) \tag{A2}$$

where $\bar{U}$ is the admissible displacement space. This equation is solved by enforcing periodic displacement boundary conditions on the paired nodes on the opposite edges of the unit cell.

A microstructural buckling analysis is performed to examine the buckling characteristics of microstructures when subjected to a prescribed macroscopic stress loading $\widetilde{\sigma}_{ij}$. The governing equation is

$$\int_\Omega D^s_{ijkl}\frac{\partial\phi_i}{\partial x_j}\frac{\partial w_k}{\partial x_l}d\Omega-P\int_\Omega\sigma_{ij}\frac{\partial\phi_m}{\partial x_i}\frac{\partial w_m}{\partial x_j}d\Omega=0,\quad \forall w_i\in\bar{W}\quad (i,j,k,l,m=1,2) \tag{A3}$$

where $\bar{W}$ is the admissible displacement space meeting the Floquet-periodic boundary condition, $P$ represents the eigenvalue which relates to the $i$th-order bifurcation buckling loads in terms of $\hat{\sigma}_k=P_k\left|\widetilde{\boldsymbol{\sigma}}\right|$, $\phi_i$ is the associated eigen-mode, and $\sigma_{ij}$ is the initial microstructural stress before the buckling arises as

$$\sigma_{ij}=\left((D_0)_{ijkl}-(D_0)_{ijkl}\frac{\partial u_p^{kl}}{\partial x_q}\right)\widetilde{\varepsilon}_{kl},\quad (i,j,k,l,p,q=1,2) \tag{A4}$$

where $\widetilde{\varepsilon}_{kl}$ is the macroscopic strain field, which is obtained by $\widetilde{\varepsilon}_{kl}=\left(D^H_{ijkl}\right)^{-1}\widetilde{\sigma}_{ij}$.

To capture all possible local and non-local buckling modes, the instability equation (A3) is solved by enforcing the Floquet-Bloch boundary condition, which is stated by

$$\phi_m(\boldsymbol{x}+\boldsymbol{R}_j)=\phi_m(\boldsymbol{x})e^{i\boldsymbol{k}\cdot\boldsymbol{R}_j},\quad (j,m=1,2) \tag{A5}$$

where $i^2=-1$, $\boldsymbol{x}=\{x,\ y\}^T$ belongs to the cell edges, $\boldsymbol{k}=(k_1,\ k_2)^T$ is the wave vector and $\boldsymbol{R}_j$ are the primitive lattice vectors which are $\boldsymbol{R}_1=(L,0)^T$ and $\boldsymbol{R}_2=(0,L)^T$ for the square unit cell, with $L$ for the edge length of the unit cell. In the analysis, $\boldsymbol{k}$ is swept over the boundaries of the first Brillouin zone due to symmetries, as shown in Fig. A1. Totally 99 wave vectors are swept.

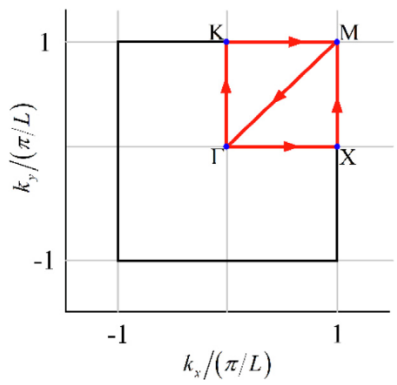


**Fig. A1.** Brillouin zone for the square unit cell. The angles indicate the sweeping order, which starts from Γ.

## Appendix B. Mesh sensitivity analysis

Mesh convergence study is conducted to examine the numerical accuracy by using different number of elements in the width direction of struts and by using different types of elements. The influence of the element numbers on both the effective stiffness and buckling strength are presented in Fig. B1a and B1b. The results show that using at least 6 layers of elements in the width direction can obtain high accuracy, where putting another layer of elements can generate marginal improvement of accuracy. The influence of the element types on the effective stiffness is presented in Fig. B1c. The results show that using 3-node linear triangular elements yields slightly larger stiffness with minor difference compared to the second-order elements.

## Appendix C. Buckling results for biaxial loading

Figs. C1 and C2 present the buckling characteristics for the Iso-HMs and SMs with rectangular holes, subjected to uniaxial and biaxial compressive stresses, respectively.

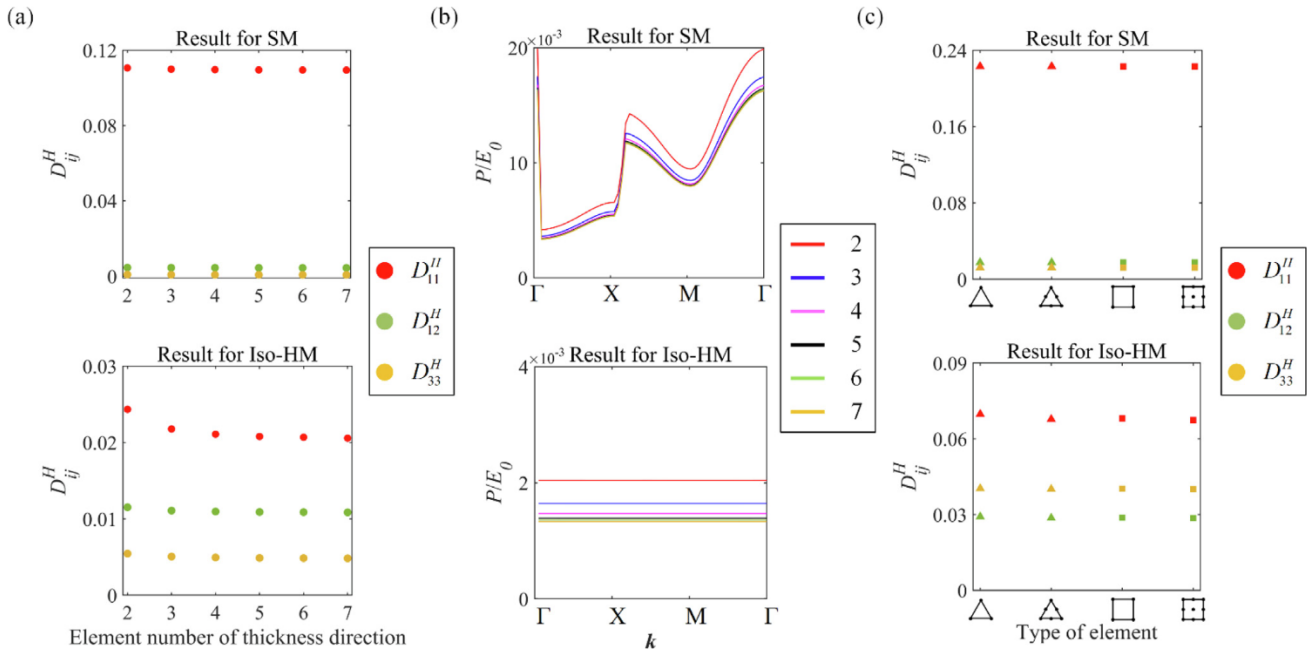


**Fig. B1.** Results for mesh sensitivity analysis, including the influence of different element numbers in the direction of strut width on (a) the effective stiffness and (b) the buckling strength; and (c) the influence of various types of elements on the effective stiffness, including the 3-node linear triangular elements, 6-node second-order triangular elements, 4-node linear quadratic elements, and second-order Lagrangian quadratic elements. The results are for both (top) the Iso-HMs and (bottom) corresponding SMs. The results in (a) and (b) are obtained by using linear triangular elements on the Iso-HMs in Fig. 9d, and those in (c) are obtained by using at least 6 layers of elements in the width direction on the Iso-HMs in Fig. 5 with $\rho$ = 38.36%.

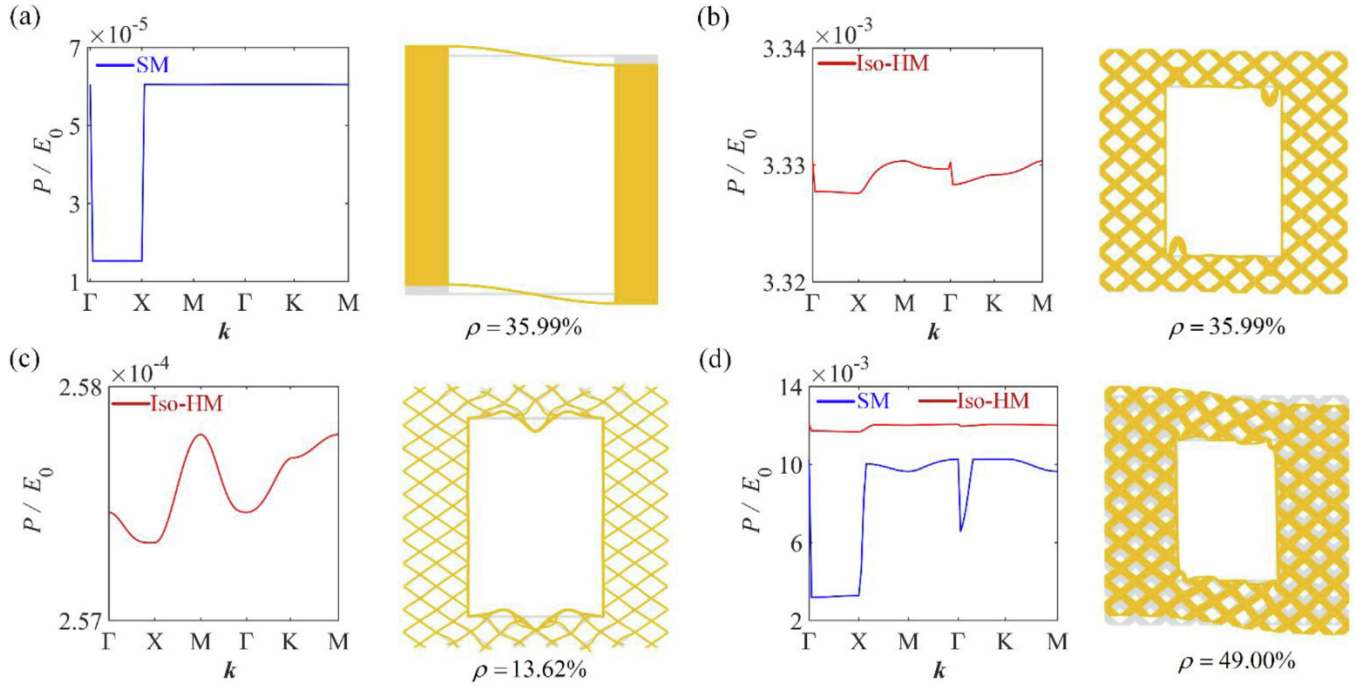


**Fig. C1.** Buckling characteristics of the Iso-HMs and SMs with rectangular holes of $R_H = 1.5$ subjected to $\tilde{\boldsymbol{\sigma}} = [-1 \quad 0 \quad 0]^T$, for (a) the SM with $\rho = 42.10\%$ and (b)-(d) Iso-HMs with various $\rho$.

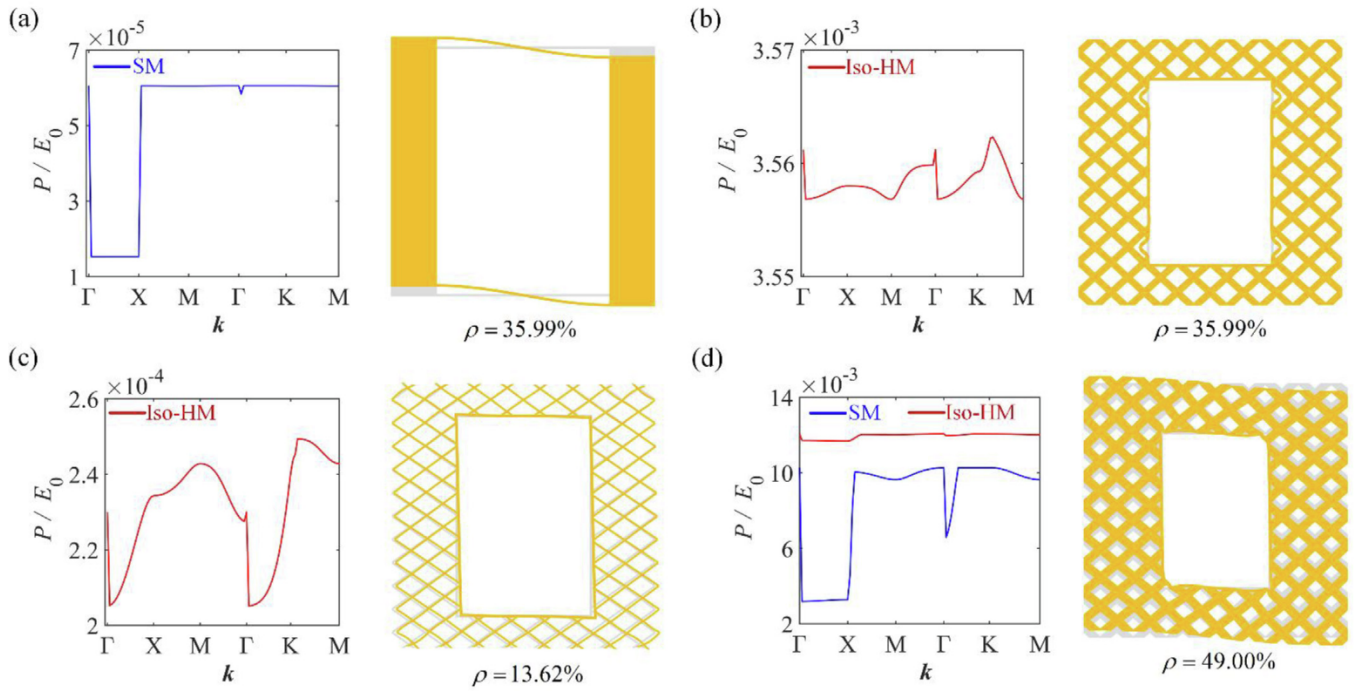


**Fig. C2.** Buckling characteristics of Iso-HMs and SMs with rectangular holes of $R_H = 1.5$ subjected to $\tilde{\boldsymbol{\sigma}} = [-1 \quad -1 \quad 0]^T$, for (a) the SM with $\rho = 42.10\%$ and (b)-(d) Iso-HMs with various $\rho$.

## Appendix D. Material property of the base material

Three square prism specimens were 3D printed, each with a section size of 3 mm and a height of 30 mm (Fig. D1a). The density of each specimen was obtained by measuring the weight and then divided by its volume, and the density of the base material was obtained as the average of the densities from the three specimens. Each specimen was loaded and unloaded four times (Fig. D1b), and its compression stiffness was obtained as the average of unloading slopes of the last three times. To this end, $E_0$ of the base material was then the average of compression stiffness of the three specimens.

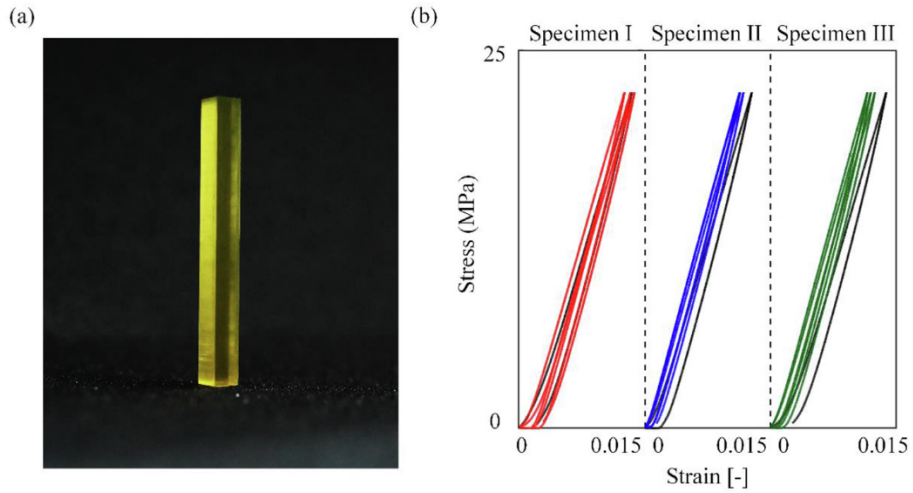


**Fig. D1.** Measurement of stiffness of the base material. (a) One 3D-printed square prism specimen; and (b) loading–unloading curves for the three specimens.

## References


[1] M. Kadic, G.W. Milton, M. van Hecke, M. Wegener, 3D metamaterials, Nature Reviews, Physics 1 (2019) 198–210.
[2] X. Zhang, Y. Wang, B. Ding, X.Y. Li, Design, Fabrication, and Mechanics of 3D Micro-/Nanolattices, Small 16 (2020) 1902842.
[3] J.U. Surjadi, L.B. Gao, H.F. Du, X. Li, X. Xiong, X.L. Fang, Y. Lu, Mechanical metamaterials and their engineering applications, Adv. Eng. Mater. (2019) 1800864.
[4] T. Bückmann, N. Stenger, M. Kadic, J. Kaschke, A. Frölich, T. Kennerknecht, C. Eberl, M. Thiel, M. Wegener, Tailored 3D mechanical metamaterials made by dip-in direct-laser-writing optical lithography, Adv. Mater. 24 (2012) 2710–2714.
[5] A. Clausen, F. Wang, J.S. Jensen, O. Sigmund, J.A. Lewis, Topology optimized architectures with programmable poisson's ratio over large deformations, Adv. Mater. 27 (2015) 5523–5527.
[6] L.R. Meza, S. Das, J.R. Greer, Strong, lightweight, and recoverable three-dimensional ceramic nanolattices, Science 345 (2014) 1322–1326.
[7] M. Kadic, T. Bückmann, N. Stenger, M. Thiel, M. Wegener, On the practicability of pentamode mechanical metamaterials, Appl. Phys. Lett. 100 (2012) 191901.
[8] Z.Y. Li, Z. Luo, L.C. Zhang, C.H. Wang, Topological design of pentamode lattice metamaterials using a ground structure method, Mater. Des. 202 (2021) 109523.
[9] T. Frenzel, M. Kadic, M. Wegener, Three-dimensional mechanical metamaterials with a twist, Science 358 (2017) 1072–1074.
[10] L. Meng, J. Shi, C. Yang, T. Gao, Y. Hou, L. Song, D. Gu, J. Zhu, P. Breitkopf, W.H. Zhang, An emerging class of hyperbolic lattice exhibiting tunable elastic properties and impact absorption through chiral twisting, Extreme Mech. Lett. 40 (2020) 100869.
[11] Y.Q. Wang, O. Sigmund, Quasiperiodic mechanical metamaterials with extreme isotropic stiffness, Extreme Mech. Lett. 34 (2020) 100596.
[12] G.A. Francfort, F. Murat, Homogenization and optimal bounds in linear elasticity, Arch. Ration. Mech. Anal. 94 (1986) 307–334.
[13] J. Berger, H. Wadley, R. McMeeking, Mechanical metamaterials at the theoretical limit of isotropic elastic stiffness, Nature 543 (2017) 533–537.
[14] T. Tancogne-Dejean, M. Diamantopoulou, M.B. Gorji, C. Bonatti, D. Mohr, 3D Plate-Lattices: An emerging class of low-density metamaterial exhibiting optimal isotropic stiffness, Adv. Mater. 30 (2018) 1803334.
[15] Z. Chen, Y. Xie, X. Wu, Z. Wang, Q. Li, S. Zhou, On hybrid cellular materials based on triply periodic minimal surfaces with extreme mechanical properties, Mater. Des. 183 (2019) 108109.
[16] R.M. Latture, M.R. Begley, F.W. Zok, Design and mechanical properties of elastically isotropic trusses, J. Mater. Res. 33 (3) (2018) 249–263.
[17] T. Tancogne-Dejean, D. Mohr, Elastically-isotropic elementary cubic lattices composed of tailored hollow beams, Extreme Mech. Lett. 22 (2018) 13–18.
[18] Q. Ma, L. Zhang, M.Y. Wang, Elastically isotropic open-cell uniform thickness shell lattices with optimized elastic moduli via shape optimization, Mater. Des. 215 (2022) 110426.
[19] C. Soyarslan, V. Blümer, S. Bargmann, Tunable auxeticity and elastomechanical symmetry in a class of very low density core-shell cubic crystals, Acta Mater. 177 (2019) 280–292.
[20] J.E. Cadman, S. Zhou, Y. Chen, Q. Li, On design of multi-functional microstructural materials, J. Mater. Sci. 48 (2013) 51–66.
[21] O. Sigmund, S. Torquato, Design of smart composite materials using topology optimization, Smart Mater. Struct. 8 (3) (1999) 365.
[22] A. Radman, X.D. Huang, Y.M. Xie, Topological optimization for the design of microstructures of isotropic cellular materials, Eng. Optim. 45 (2013) 1331–1348.
[23] L. Xia, P. Breitkopf, Design of materials using topology optimization and energy-based homogenization approach in Matlab, Struct. Multidiscip. Optim. 52 (2015) 1229–1241.
[24] X.D. Huang, A. Radman, Y.M. Xie, Topological design of microstructures of cellular materials for maximum bulk or shear modulus, Comput. Mater. Sci 50 (2011) 1861–1870.
[25] O. Sigmund, A new class of extremal composites, J. Mech. Phys. Solids 48 (2) (2000) 397–428.
[26] H.K. Zhang, Z. Kang, Y.Q. Wang, W.J. Wu, Isotropic "Quasi-Fluid" metamaterials designed by topology optimization, Advanced Theory and Simulations 3 (2020) 1900182.
[27] O. Sigmund, Tailoring materials with prescribed elastic properties, Mech. Mater. 20 (1995) 351–368.
[28] W. Chen, D. Ruan, X.D. Huang, Optimization for twist chirality of structural materials induced by axial strain, Materials Today, Communications 15 (2018) 175–184.
[29] L. Zhang, Z. Hu, M.Y. Wang, S. Feih, Hierarchical sheet triply periodic minimal surface lattices: Design, geometric and mechanical performance, Mater. Des. 209 (2021) 109931.
[30] H.K. Zhang, W.J. Wu, Z. Kang, X.Q. Feng, Topology optimization method for the design of bioinspired self-similar hierarchical microstructures, Comput. Methods Appl. Mech. Eng. 372 (2020) 113399.
[31] S.H. Siddique, P.J. Hazell, H.X. Wang, J.P. Escobedo, A.A.H. Ameri, Lessons from nature: 3D printed bio-inspired porous structures for impact energy absorption - A review, Addit. Manuf. 58 (2022) 103051.
[32] L. Zhang, Q.P. Ma, J.H. Ding, S. Qu, J. Fu, M.W. Fu, X. Song, M.Y. Wang, Design of elastically isotropic shell lattices from anisotropic constitutive materials for additive manufacturing, Addit. Manuf. 59 (2022) 103185.
[33] B. Hanks, J. Berthel, M. Frecker, T.W. Simpson, Mechanical properties of additively manufactured metal lattice structures: Data review and design interface, Addit. Manuf. 35 (2020) 101301.
[34] X.Y. Zheng, W. Smith, J. Jackson, B. Moran, H. Cui, D. Chen, J. Ye, N. Fang, N. Rodriguez, T. Weisgraber, C.M. Spadaccini, Multiscale metallic metamaterials, Nat. Mater. 15 (10) (2016) 1100–1106.
[35] S. Yin, H. Chen, J. Li, T. Yu, J. Xu, Effects of architecture level on mechanical properties of hierarchical lattice materials, Int. J. Mech. Sci. 157 (2019) 282–292.
[36] P.Q. Liu, B.T. Sun, J.K. Liu, L. Lu, Parametric shell lattice with tailored mechanical properties, Additive Manufacturing In press (2022) 103258.
[37] E. Mazur, I. Shishkovshy, Additively manufactured hierarchical auxetic mechanical metamaterials, Materials 15 (2022) 5600.
[38] D. Mousanezhad, S. Babaee, H. Ebrahimi, R. Ghosh, A.S. Hamouda, K. Bertoldi, A. Vaziri, Hierarchical honeycomb auxetic metamaterials, Sci. Rep. 5 (2016) 18306.
[39] L. Shen, X. Wang, Z. Li, K. Wei, Z. Wang, Elastic properties of an additive manufactured three-dimensional vertex-based hierarchical re-entrant structure, Mater. Des. 216 (2022) 110527.
[40] A. Mrozek, T. Strek, Numerical analysis of dynamic properties of an auxetic structure with rotating squares with holes, Materials 15 (2022) 8712.
[41] L.H. Chen, Y. Li, B.L. Su, Hierarchy in materials for maximized efficiency, Natl. Sci. Rev. 7 (2020) 1626–1630.
[42] K.K. Dudek, J.A.I. Martinez, G. Ulliac, M. Kadic, Micro-Scale auxetic hierarchical mechanical metamaterials for shape morphing, Adv. Mater. 34 (2022) e2110115.
[43] H.S. Ngoc, M.P. Thong, T.T. Tung, H. Hao, G.X. Lu, Mechanical properties and energy absorption of bio-inspired hierarchical circular honeycomb, Compos. B Eng. 236 (2022) 109818.

[44] Z. Zhang, Y. Zhang, H.J. Gao, On optimal hierarchy of load-bearing biological materials, Proceedings of the Royal Society B: Biological Sciences 278 (1705) (2011) 519-525.
[45] L.R. Meza, A.J. Zelhofer, N. Clarke, A.J. Mateos, D.M. Kochmann, J.R. Greer, Resilient 3D hierarchical architected metamaterials, Proceedings of the National Academy of Sciences 112 (2015) 11502-11507.
[46] Y. Chen, T. Li, Z. Jia, F. Scarpa, C. Yao, L. Wang, 3D printed hierarchical honeycombs with shape integrity under large compressive deformations, Mater. Des. 137 (2018) 226–234.
[47] C.R. Thomsen, F.W. Wang, O. Sigmund, Buckling strength topology optimization of 2D periodic materials based on linearized bifurcation analysis, Comput. Methods Appl. Mech. Eng. 339 (2018) 115–136.
[48] P. Pedersen, On optimal orientation of orthotropic materials, Structural Optimization 1 (2) (1989) 101–106.
[49] M.P. Bendsøe, N. Kikuchi, Generating optimal topologies in structural design using a homogenization method, Comput. Methods Appl. Mech. Eng. 71 (2) (1988) 197–224.
[50] L. Xia, P. Breitkopf, Design of materials using topology optimization and energy-based homogenization approach in Matlab, Struct. Multidiscip. Optim. 52 (6) (2015) 1229–1241.
[51] E. Andreassen, C.S. Andreasen, How to determine composite material properties using numerical homogenization, Comput. Mater. Sci 83 (2014) 488–495.
[52] E. Andreassen, B.S. Lazarov, O. Sigmund, Design of manufacturable 3D extremal elastic microstructure, Mech. Mater. 69 (2014) 1–10.
[53] S.I. Ranganathan, M. Ostoja-Starzewski, Universal elastic anisotropy index, Phys. Rev. Lett. 101 (2008) 055504.
[54] M.N. Andersen, Y.Q. Wang, F.W. Wang, O. Sigmund, Buckling and yield strength estimation of architected materials under arbitrary loads, Int. J. Solids Struct. 254 (2022) 111842.
[55] H.L. Fan, F.N. Jin, D.N. Fang, Uniaxial local buckling strength of periodic lattice composites, Mater. Des. 30 (2009) 4136–4145.
[56] F.W. Wang, O. Sigmund, Architecting materials for extremal stiffness, yield and buckling strength, arXiv preprint arXiv:2210.00003 (2022).